

Generation of turbulent inflow data from realistic approximations of the covariance tensor

Cite as: Phys. Fluids **34**, 115140 (2022); <https://doi.org/10.1063/5.0106664>

Submitted: 29 June 2022 • Accepted: 18 October 2022 • Accepted Manuscript Online: 22 October 2022 • Published Online: 15 November 2022

Published open access through an agreement with JISC Collections

 Muting Hao (郝苜婷),  Joshua Hope-Collins and  Luca di Mare



View Online



Export Citation



CrossMark

ARTICLES YOU MAY BE INTERESTED IN

[Numerical investigation and parametric analysis of an attached eddy model applied to inlet condition](#)

Physics of Fluids **34**, 115143 (2022); <https://doi.org/10.1063/5.0122737>

[Large-eddy simulation study of rotating detonation supersonic turbine nozzle generated by the method of characteristics under oscillating incoming flow](#)

Physics of Fluids **34**, 116119 (2022); <https://doi.org/10.1063/5.0111900>

[Unsupervised deep learning of spatial organizations of coherent structures in a turbulent channel flow](#)

Physics of Fluids **34**, 115138 (2022); <https://doi.org/10.1063/5.0123555>



Physics of Fluids

Special Topic: Paint and Coating Physics

Submit Today!

Generation of turbulent inflow data from realistic approximations of the covariance tensor

Cite as: Phys. Fluids **34**, 115140 (2022); doi: [10.1063/5.0106664](https://doi.org/10.1063/5.0106664)

Submitted: 29 June 2022 · Accepted: 18 October 2022 ·

Published Online: 15 November 2022



View Online



Export Citation



CrossMark

Muting Hao (郝苗婷),^{a)} Joshua Hope-Collins, and Luca di Mare

AFFILIATIONS

Oxford Thermo-Fluids Institute, Department of Engineering Science, University Of Oxford, Oxford OX2 0ES, United Kingdom

^{a)} Author to whom correspondence should be addressed: muting.hao@stcatz.ox.ac.uk

ABSTRACT

This study presents a novel synthetic inflow generator capable of producing a random field matching a realistic set of two-point statistics with minimal input. The method is based on two main elements. The first element is a procedure to infer realistic two-point covariance tensors from readily available data (e.g., freestream velocity, boundary layer thickness, and turbulence intensity) by a preliminary Reynolds-averaged Navier–Stokes simulation with an explicit algebraic Reynolds stress model closure. The second element is an efficient eigen-decomposition step of the two-point correlation tensor, which determines a set of modes. The modal decomposition guarantees the spatial correlation in transversal directions, while the temporal correlation/streamwise spatial correlation is obtained by digital filters based on longitudinal and transversal spectra of a realistic shape and Taylor’s hypothesis. The instantaneous inlet flow field is obtained by a linear combination of the modes via uncorrelated random weights with unit variance. The modes are generated in a computationally inexpensive pre-processing step. Compared to existing inflow generation methods that try to match given two-point statistics, the proposed method relieves the burden of obtaining data from direct numerical simulation (DNS) or experiments, while the complexity of the eigenvalue problem that needs to be solved is reduced. The proposed method is shown to produce a realistic turbulent channel flow and a realistic turbulent boundary layer by the large-eddy simulation, which contains statistics that are in good agreement with results from DNS. The proposed inflow generator features, cost-effectiveness, robustness, and potential for generalization to complex geometries.

© 2022 Author(s). All article content, except where otherwise noted, is licensed under a Creative Commons Attribution (CC BY) license (<http://creativecommons.org/licenses/by/4.0/>). <https://doi.org/10.1063/5.0106664>

I. INTRODUCTION

A. Turbulent inflow generation method

The advancement of the computer power has made scale-resolving simulation techniques such as direct numerical simulation (DNS)^{1,2} or large-eddy simulation (LES)^{3–5} applicable to flows of practical interest. The accuracy of these simulations relies on the resolution as well as accurate boundary data. This is especially true for the inflow boundary, where a realistic inlet turbulent flow field is necessary.

Previous studies have proved that simulated mean flow and turbulent profiles are highly sensitive to the properties of the inlet flow field. An unrealistic inlet flow field might cause the flow to re-laminarize or might cause the boundary layer to readjust over a long section of the domain, thereby requiring a longer domain for a given simulation. Therefore, a high-quality time-dependent inflow boundary condition is a necessary component for simulating spatially developing flows. Similar problems are faced by hybrid RANS-LES methods at the interface between the RANS and the LES domains.^{6–8}

Generating a turbulent inflow requires a time series containing all the length and timescales resolved by the simulation on the inflow surface. A number of methods have been studied for obtaining fully turbulent inflow data. These methods can be categorized into four groups:⁹ (i) transition-inducing methods,^{10–17} which introduce deliberate perturbations in the flow to trigger transition; (ii) turbulence library-based methods, which extract realistic inflow data from a database of snapshots or an auxiliary simulation; (iii) recycling–rescaling methods,^{18–20} which generate inflow data by rescaling the flow field at a suitable downstream location; and (iv) synthetic inflow generators, which rely on random sequences to generate inflow data. Among these four general methods, (i) is not very practical because of the lack of generality and the need for a large development length—as much as 50 boundary layer thicknesses¹⁷—to allow for the transitional flow to develop. Method (iii) requires special techniques²¹ to handle spurious low-frequency signals induced by the finite distance between the recycling station and the inlet surface.^{18,21,22} (ii) and (iv) are preferable and combined in this study.

Library-based methods are superior in terms of reproducing correct phase information as they use a realistic data source. When the data source is close to the target geometry/operating configuration, this method can faithfully generate realistic inflow data.

For complex geometries or industrial applications, it may be difficult to setup auxiliary simulations with periodic boundaries and no source of library data may be available. As a consequence, synthetic inflow generations are the method of choice for general flow configurations.

The earliest example of a synthetic inflow consists in superimposing random disturbances on a laminar profile²³ for a turbulent jet simulation. The main difficulty in constructing synthetic inflow methods is the generation of random sequences that exhibit realistic correlations in both time and space. Different synthetic inflow generators differ in the way they enforce spatial and temporal coherence in the inflow signal.

The temporal correlation was first considered when Hanna *et al.*²⁴ obtained required timescales along with turbulence intensities in an LES simulation by scaling a base time series. A temporal correlation of exponential shape was enforced. The accuracy of resulting inlet data was still doubtful due to a lack of spatial correlations. Kondo²⁵ and Lee²⁶ showed that both spatial and temporal correlations can be preserved when the energy spectrum is prescribed during inverse Fourier transform (IFT). When being used for recovering realistic turbulence, however, the IFT may need a long development distance, which can be as much as 20 boundary layer thickness as shown in Le *et al.*²⁷

Batten's⁶ synthesizing reproduced the imposed length correlation, time correlation, and all second moments, via tensor scaling at the RANS-to-LES interface. In Jarrin *et al.*'s⁷ synthetic-eddy method (SEM) and its variants, the superimposed coherent structures satisfy two-point correlations that are provided in the overlapping zone of the hybrid RANS-LES simulations. However, Batten's method features slow redevelopment, as is shown being more than 20 channel half-heights, indicated in Keating.²⁸ Jarrin's SEM requires around two to four times the boundary layer thickness²⁹ for the RANS-to-LES transition.

The spectral approaches rely on the properties of Fourier transforms to enforce correlations in space and time. Spectral approaches exploit homogeneous directions and Taylor's hypothesis in order to represent the inflow data as Fourier series in space and time. The Fourier representation of the inflow field makes the introduction of a realistic energy spectrum straightforward. As an example, the random flow generation (RFG) method by Smirnov *et al.*³⁰ operates by superimposing harmonic functions with random factors in amplitude and phase. The resulting fluctuations feature the prescribed energy spectrum, turbulence length scales, and timescales. The method requires as input an energy spectrum, which is a function of the wave number only.

POD offers a rigorous mathematical framework for the description of spatially and temporally coherent structures in a turbulence field. POD has been used³¹ for synthetic turbulence generation. POD is attractive because of its optimality properties, which allow a given flow field to be represented with the smallest number of modes, for a given accuracy.³² However, since POD necessitates a predetermined dataset, for example, from experiments, DNS, or adequately resolving simulations, POD-based methods have not met wide acceptance so far.

The digital filter-based method is a way of generating correlated signals with prescribed length scales. The prescribed value is known from experiments or from heuristic estimates, and the filtering operation imposes these correlated length scales in the originally random noise. Klein's³³ approach to generating a synthetic inflow is filtering an uncorrelated random series with zero mean and unit variance by a set of filter coefficients that are solved by matching different two-point correlation forms. Xie and Castro³⁴ used an exponential function instead of the Gaussian function assumed by Klein³³ to improve the accuracy of the second correlation function. In terms of generalization to 3D, a cost-effective 2D filtering was promoted³⁴ instead of the convolution of 1D. These methods assumed a constant timescale as input for the whole inlet. Additional treatment, separating the inlet into zones, was thus required to vary lateral and vertical length scales. More straightforward strategies are needed. Hoepffner³⁵ tried a novel filtering in the form of an autoregressive linear filter, the coefficients of which are solved from the Yule-Walker equation to ensure the required spatial and temporal correlations. They need to rely on DNS and a long spatial simulation domain for the transition to turbulence to occur or a small amount of noise to extract statistics of the instability of the mixing layer as a reference. However, these methods have shown potential for exploring simpler and more straightforward filtering ways, which can vary timescales.

An ideal turbulence boundary condition should satisfy a few requirements: cost-effectiveness, applicability to spatially inhomogeneous flows, lack of spurious signals, and on-the-fly generation of the inflow data. Although most methods mentioned above have attained success in a certain range of applications, they more or less fail to meet all the expectations from an ideal inflow condition. As an example, methods in (i)–(iii), and those synthesizers, which have been shown to require relatively long development length, cannot be used in complex cases of practical interest because of the high computational cost.

An effective synthetic turbulence method can be devised if an inexpensive way of generating two-point correlation tensors can be found and if the information contained in the two-point correlations can be incorporated directly into the inflow data.

Based on these considerations, we propose a turbulence synthesizing method, which combines the library-based method, POD, and the digital-filter method. The proposed method is capable of producing a random field matching a realistic set of two-point statistics with minimal input. The method operates in four steps. In the first step, an inexpensive preliminary Reynolds averaged Navier–Stokes (RANS) calculation is used to obtain the mean flow, turbulent kinetic energy (TKE), and Reynolds stress distributions on the inflow surface, together with a length-determining quantity. The RANS simulation operates in a way reminiscent of the precursor simulation in a library-based method, but it can be performed at a negligible computational cost. The RANS simulation is the data source of our proposed synthetic turbulence generator (see Sec. II A). In the second step, the RANS data are used to construct approximate two-point covariance tensors on the inlet surface (see Sec. II B). In the third step, a POD is performed on the approximate tensors to obtain an orthonormal basis for the flow quantities on the inflow surface. If the flow has a homogeneous direction, a Fourier representation is used along that direction. The POD and Fourier modes describe the variation of the inflow

signal on the inflow surface and are responsible for preserving two-point correlations on that surface (see Sec. II B). In the fourth and final step, a digital filter is constructed for each POD/Fourier mode and describes the variation of the inflow signal in time. The digital filters are responsible for enforcing two-time correlations (see Sec. II B). These steps are only performed once prior to the start of the main LES simulation. At each time step of the LES simulation, a new realization of the inflow field is generated by the convolution of the previously constructed space–time filters with an uncorrelated random sequence or an interpolation algorithm.

The four steps of the proposed method are presented in detail in Sec. II. Section III describes the LES flow solver used for the main simulation and the way of implementing the proposed synthetic inflow generator before and during the LES running. Results and discussions are presented for a channel (see Sec. IV) and a developing boundary layer (see Sec. V). Section IV presents comparisons with both DNS data and LES results by using the periodic boundary condition. Mean velocity profiles and Reynolds normal and Reynolds shear stresses are examined for the purpose of validation. The effects of inflow parameters on a developing boundary layer are shown in Sec. V. Section V presents guidance on the selection of the method parameters for new users who are interested in using the proposed synthetic inflow generator. Finally, conclusions and recommendations for future work are presented in Sec. VI.

II. METHODOLOGY

The design of a turbulence generator consists in identifying and reproducing certain statistics.

A. Identifying statistics

Statistics are both treated as input and output of the generated turbulence. As for the way to correctly determine the statistics for use, previous studies on synthetic generation have taken into account at least one of the spatial correlations, temporal correlations, and the Reynolds stress tensor.

Early examples of them are utilizing preliminary experimental data. With experimentally determined time series, Bonnet *et al.*^{31,36} defined correlation functions from experiments and built their inflow condition on a mixing layer.

Their success confirmed that introducing correlations using library-based methods is feasible. To get rid of the high cost of experiments, this study expects to find an equivalent numerical precursor that provides information about correlations. In addition, the precursor simulations in all the methods published so far are themselves either DNS or LES. Even though for just the precursor, they use high-fidelity codes to get statistics at the cost of a certain amount of computational resources.

This proposed contribution aims to find a precursor and, via using filtering temporally and spatially, to prepare temporal and spatial correlations, which can be incorporated into subsequent inflow synthesizing. We expect the precursor to be realistic approximations from which trustworthy correlations can be extracted. The procedure should be able to set up case-dependent precursor simulations easily with the minimum information required. Computational expenses should be controlled to a minimum, while reliable results could be found instantly.

The statistics chosen for turbulence construction in this study is a realistic two-point covariance tensor. It contains information on the magnitudes and the spectrum of different length-scale structures. As the data source in the library-based method, a precursor is proposed to infer a realistic two-point covariance tensor from readily available information (e.g., freestream velocity, boundary layer thickness, and turbulence intensity). The precursor is a preliminary simulation based on RANS incorporated with an explicit algebraic Reynolds stress model (EARSM) closure. Mean velocities are obtained in the meantime.

B. Reconstruction

Once a suitable representation of the two-point covariance tensor is obtained from the solution to the identifying statistics, the second step is the generation of the synthetic turbulence.

Different from the synthesizing methods reviewed in Sec. I, this study will propose an eigenvalue-based synthesizing method. It will combine the advantageous features of the POD, and the filtering-based method reviewed above. The eigenvalue-based method is composed of an efficient eigendecomposition of the two-point correlation tensor, which determines a set of modes and enforces correlation in space. Time filters are applied to individual Fourier modes. Therefore, the final solution is a linear superimposing of time and space variance signals through random weights with unit variance. The computational effort will be shown to be modest.

C. Preliminary approximation of two-point statistics

In this section, the preliminary simulation is illustrated. We also show how to build the statistics, that is, the covariance tensor, which will be decomposed in Sec. II C 1, to seek the modes for the following reconstruction.

1. The precursor RANS solver

The preliminary procedure consists of establishing a RANS simulation from which statistics will be extracted and later reproduced using a filter-based reconstruction. The preliminary simulation is designed to take smaller possible computational efforts. The procedure takes a minimal set of input data that allow target flow conditions to be established. The input data include the free-stream velocity, the temperature, the pressure, the turbulence level, the desired boundary layer thickness, and the viscosity. The parameters needed to be specified for the energy spectrum and the time filtering are chosen according to experience. This study will provide some guidance for the selection of these parameters. The modeling method is a two-equation RANS model with the EARSM closure. The EARSM closure is adopted as it can approximate the anisotropy of the Reynolds stress tensor.

Note that the inflow generation procedure is described for a flow where the inlet section can be generated by a developing turbulent boundary layer, but the method of reconstructing following that can be equally well applied to any inlet configuration as long as RANS data (or higher resolution simulation data) are available.

The configuration of the preliminary simulation depends on the nature of the incoming flow. As an example, if the incoming

flow is a developing boundary layer, the preliminary simulation is based on the parabolized Navier–Stokes equations. In this case, the preliminary simulation takes the shape of a marching procedure that starts from a nominal profile far upstream of the inlet. At the start of the calculation, a one-dimensional mesh is constructed. The grids are orthogonal to the wall and just cover a height of the boundary layer thickness, with the first grid size normal to the wall as $y_0 = 0.5 \frac{N u_0}{u_0}$. The simulation is then marched until the boundary layer thickness matches the desired value. The computational domain is represented at any time during the procedure by only two consecutive streamwise stations where the wall-normal profiles of the flow quantities are computed. At each time step, the newly generated result overwrites the previous records and is written on the current virtual cell center. In this way, no more than two lines of cells are stored at any time step, without the cumbersomeness of storing the whole streamwise extent of the precursor domain. The wall-normal grid distribution is updated to adapt to the turbulent boundary layer development until the turbulent boundary layer thickness of δ_{99} or the momentum thickness of θ is satisfied. Figure 1 shows this computational domain in the two sets of coordinate systems that are used. The coordinate axes 1, 2, and 3 correspond to the coordinate axis x , y , z , denoting the streamwise, wall-normal, and spanwise directions. The former is used only in Eq. (1) for facilitating the tensor notation, while the latter is used for the rest of the equations.

Wilcox and Rubesin's³⁷ EARSM closure is adopted in the preliminary simulation. The nonlinear constitutive relation for their $k - w^2$ model is

$$\tau_{ij}^0 = -\frac{2}{3} \rho k_e \delta_{ij} + 2\mu_T \left(S_{ij} - \frac{1}{3} \frac{\partial U_k}{\partial X_k} \delta_{ij} \right) + \frac{8}{9} \frac{\rho k_e (S_{ik} \Omega_{kj} + S_{jk} \Omega_{ki})}{\beta^* \omega^2 + 2S_{mn} S_{nm}}. \quad (1)$$

This constitutive relationship in Eq. (1) can model Reynolds stresses that do not necessarily align with the mean rates of strain. This prescription for the Reynolds-stress tensor guarantees that the peak values of

$$\overline{u'^2} : \overline{v'^2} : \overline{w'^2} = 4 : 2 : 3 \quad (2)$$

for the flat-plate boundary layer. Equation (2) is a good approximation for the log layer and much of the defect layer.

For a parallel shear flow, the individual Reynolds normal stresses are specialized to

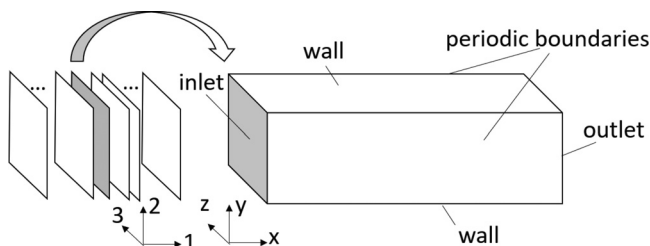


FIG. 1. The computational domain shown in two sets of coordinate systems.

$$\overline{u'^2} = \frac{2}{3} k_e \left(1 + \frac{2}{3} \frac{\left(\frac{\partial U_1}{\partial X_2} \right)^2}{\beta^* \omega^2 + \left(\frac{\partial U_1}{\partial X_2} \right)^2} \right), \quad (3)$$

$$\overline{v'^2} = \frac{2}{3} k_e \left(1 - \frac{2}{3} \frac{\left(\frac{\partial U_1}{\partial X_2} \right)^2}{\beta^* \omega^2 + \left(\frac{\partial U_1}{\partial X_2} \right)^2} \right), \quad (4)$$

$$\overline{w'^2} = \frac{2}{3} k_e. \quad (5)$$

2. Construction of a covariance tensor from mean profiles

The quick RANS calculation in Sec. II C 1 estimates mean velocity components (in three directions for 3D cases), Reynolds stresses, and length scales. We now proceed to show the construction of a covariance tensor based on this information. This is done on the inlet slice of the main computation. In general, if the inlet surface contains n grid faces, the correlation tensor contains $3n \times 3n$ entries. If a homogeneous direction is present, then the correlation tensor contains $3n \times 3n$ entries, but n is the number of cells in the wall-normal direction only. A separate correlation tensor must be generated for each Fourier mode.

The shape of the covariance tensor is not very sensitive to Re_τ ³⁸ for a given flow. As an example, in turbulent boundary layers or channel flows, a reasonable covariance tensor can therefore be constructed by assembling the following components:

$$\begin{aligned} \langle u' u' \rangle_\kappa(y_1, y_2) &= f_\kappa^0 \sqrt{\overline{u'^2}(y_1) \overline{u'^2}(y_2)} e^{-\alpha \frac{(y_1 - y_2)^2}{\ell(y_1) \ell(y_2)}}, \\ \langle v' v' \rangle_\kappa(y_1, y_2) &= f_\kappa^0 \sqrt{\overline{v'^2}(y_1) \overline{v'^2}(y_2)} e^{-\alpha \frac{(y_1 - y_2)^2}{\ell(y_1) \ell(y_2)}}, \\ \langle w' w' \rangle_\kappa(y_z, y_2) &= f_\kappa^0 \sqrt{\overline{w'^2}(y_1) \overline{w'^2}(y_2)} e^{-\alpha \frac{(y_1 - y_2)^2}{\ell(y_1) \ell(y_2)}}, \\ \langle u' v' \rangle_\kappa(y_1, y_2) &= -f_\kappa^0 \sqrt{\overline{u' v'}(y_1) \overline{u' v'}(y_2)} e^{-\alpha \frac{(y_1 - y_2)^2}{\ell(y_1) \ell(y_2)}}, \end{aligned} \quad (6)$$

where κ is the spanwise Fourier index mode, y_1 and y_2 are two wall-normal positions, and u' , v' , w' are turbulent velocities in three directions. In Eq. (6), a square root function and a Gaussian shape function are used to ensure that, first, the reconstructed covariance tensor is smooth; second, the Reynolds stresses appear on the main diagonal of the covariance tensor. The entries of the covariance tensor are prescribed from heuristic arguments in the physical space. The covariance tensor is a symmetric matrix. $\langle u' w' \rangle$, $\langle v' w' \rangle$ are assigned as zero, because the corresponding Reynolds stresses in the homogeneous directions are zero. Therefore, to build the final combined covariance tensor, only the four sets of components in Eq. (6) are needed to know. The covariance tensor is arranged in Eqs. (7) and (8) as below:

$$\begin{aligned}
 R_{uu} &= \begin{bmatrix} u'_1 u'_1 & u'_1 u'_2 & \cdots & u'_1 u'_n \\ u'_2 u'_1 & u'_2 u'_2 & \cdots & u'_2 u'_n \\ \vdots & \vdots & \ddots & \vdots \\ u'_n u'_1 & u'_n u'_2 & \cdots & u'_n u'_n \end{bmatrix} \in \mathbb{R}^{n \times n}, \\
 R_{ww} &= \begin{bmatrix} w'_1 w'_1 & w'_1 w'_2 & \cdots & w'_1 w'_n \\ w'_2 w'_1 & w'_2 w'_2 & \cdots & w'_2 w'_n \\ \vdots & \vdots & \ddots & \vdots \\ w'_n w'_1 & w'_n w'_2 & \cdots & w'_n w'_n \end{bmatrix} \in \mathbb{R}^{n \times n}, \\
 R_{vv} &= \begin{bmatrix} v'_1 v'_1 & v'_1 v'_2 & \cdots & v'_1 v'_n \\ v'_2 v'_1 & v'_2 v'_2 & \cdots & v'_2 v'_n \\ \vdots & \vdots & \ddots & \vdots \\ v'_n v'_1 & v'_n v'_2 & \cdots & v'_n v'_n \end{bmatrix} \in \mathbb{R}^{n \times n}, \\
 R_{uv} &= \begin{bmatrix} u'_1 v'_1 & u'_1 v'_2 & \cdots & u'_1 v'_n \\ u'_2 v'_1 & u'_2 v'_2 & \cdots & u'_2 v'_n \\ \vdots & \vdots & \ddots & \vdots \\ u'_n v'_1 & u'_n v'_2 & \cdots & u'_n v'_n \end{bmatrix} \in \mathbb{R}^{n \times n}.
 \end{aligned} \tag{7}$$

The final covariance tensor is assembled from these individual matrices following the arrangement of $3n \times 3n$ as the following equation:

$$M = \begin{bmatrix} R_{uu} & R_{uw} & R_{uv} \\ R_{uw}^\top & R_{ww} & R_{vw} \\ R_{uv}^\top & R_{vw}^\top & R_{vv} \end{bmatrix}, \tag{8}$$

where n is the number of nodes in the wall-normal direction on the inlet slice.

D. Reconstruction by eigenmodes

1. Eigenmode space

The covariance tensor prescribed in the physical space can be interpreted in the eigenmode space. The eigenvectors of the covariance matrix are taken as an alternative basis for the representation of the covariance tensor. The reason why a transformation from the physical space to the eigenmode space is needed can be explained as follows. First, it is easier to generate an uncorrelated signal by a random number generator (shown in Sec. IID 1 a); the eigenmode space allows an uncorrelated signal to be combined into a known correlation tensor based on the mean flow and the length scales in Eq. (6). Second, via transformation, it is possible to make the eigenvalues positive and real, which is essential for a correlation tensor. The current procedure should guarantee that the guessed correlation tensor is Hermitian because of the way it is constructed, but the positivity has not been guaranteed for all eigenvalues. In fact, a small number of negative eigenvalues are ordinarily created. These appear in the tail end of the spectrum and represent a small fraction of the whole turbulent kinetic energy. These modes are not realizable; that is, it is not possible to

determine a set of spatial patterns that when combined through a random uncorrelated signal will give correlation patterns associated with these modes. For this reason, they are suppressed by setting the corresponding eigenvalues to zero. Imposing a cutoff in the number of modes is generally sufficient to remove all the unrealizable modes.

a. Reconstruction via a correlated random sequence generator. A method of creating a correlated random sequence is shown below. Assuming x_i^* is the output as an uncorrelated random variable, which satisfies the property of zero mean and unit variance, that is, $\langle x_i^* \rangle = 0$, $\langle x_i^* x_j^* \rangle = \delta_{ij}$, let

$$y_i^* = p_{ij} x_j^* \tag{9}$$

be a new set of random variables, with the covariance being

$$\langle y_i^* y_j^* \rangle = p_{ih} p_{jk} \langle x_h^* x_k^* \rangle = p_{ih} p_{jk} = q_{ij}. \tag{10}$$

If q_{ij} is a given covariance tensor, and its symmetric factorization $q_{ij} = s_{ih}^* s_{jh}^*$ is known, the second set of random sequence can be conversely treated as

$$y_i^* = s_{ih}^* x_h^*, \tag{11}$$

whose covariance tensor will be q_{ij} . Conversely, a correlated random variable y_i^* can be produced by an uncorrelated random variable x_h^* and the factorization of a prescribed symmetric covariance tensor matrix q_{ij} . In this way, the problem of converting an uncorrelated sequence to a correlated random sequence is reduced to a problem of symmetric factorization. A suitable factorization is the eigenvalue decomposition.

b. Energy cutoff. In our case, each eigenvector is $3n$ entries long, with u' components in the first n rows, v' components in the second n rows, and w' components in the last n rows. An additional advantage of a decomposition of the correlation tensor in eigenmodes is that not only negative generated eigenmodes can be suppressed, but also a few modes are necessary to be retained for most of the turbulent kinetic energy. This modal decomposition property reduces the computational effort required to generate a realistic inlet flow field. A minimum number of eigenvalues are preserved according to the cutoff criteria of total energy. Namely, only leading eigenvalues and their corresponding eigenvectors should be preserved. The total turbulence energy of preserved decomposed eigenmodes hereby should just cover a given large fraction (around 92% is proved to be efficient for our case). No more than one-fifth of eigenmodes are usually needed to recover 92% of the turbulent energy. Assuming the eigenvectors are sorted in descending order, and if m is the number of the retained eigenmodes, Eq. (12) indicates that the total turbulent energy can be approximated by a truncated summation,

$$\sum_{i=0}^{3n-1} k_i |_{1 \times 3n} = \sum_{i=0}^{3n-1} |\lambda_i| \approx \sum_{i=0}^m |\lambda_i|, \tag{12}$$

where λ_i is the eigenvalue of the i th eigenmode, and k_i is the kinetic energy retained in the i th eigenmode.

c. The eigenmode reconstruction shown by a test case. The velocity on an individual point of the median plane can be constructed by

rescaling the retained eigenmodes of the correlation tensor by the square root of their corresponding eigenvalues

$$\begin{bmatrix} \hat{u}_j(y) \\ \hat{v}_j(y) \\ \hat{w}_j(y) \end{bmatrix} = \begin{bmatrix} g_1^j \\ g_2^j \\ \dots \\ g_{3n}^j \end{bmatrix} \sqrt{\lambda_j}, \quad j = 1, 2, \dots, m \quad (m \ll 3n), \quad (13)$$

where λ_j is the eigenvalue of the j th retained eigenmode, and g_i^j is the i th row of the j th eigenvector.

The reproduced signal will satisfy the prescribed mean flow quantities and length scales. This is proved by a one-dimensional case published by the same group³⁸ and a two-dimensional case in Fig. 2.

Figure 2 shows that with more eigenmodes, the reconstruction of the covariance tensor can be more accurate. When using 72 eigenmodes, the highest error is within 10% and within an ignorable area. The error between the desired and the obtained covariance is generally below 1%, while there is a 50% reduction in spectral basis size after construction.

For a three-dimensional domain, the spanwise variation of turbulence should be introduced. In principle, a similar procedure of looking for eigenvectors and eigenvalues can be proceeded in the spanwise direction to generate the genuinely two-dimensional space on each streamwise slice.

2. Fourier space

In fact, the domain of the cases we focus on in this study is symmetric and periodic in the spanwise direction. These features are not

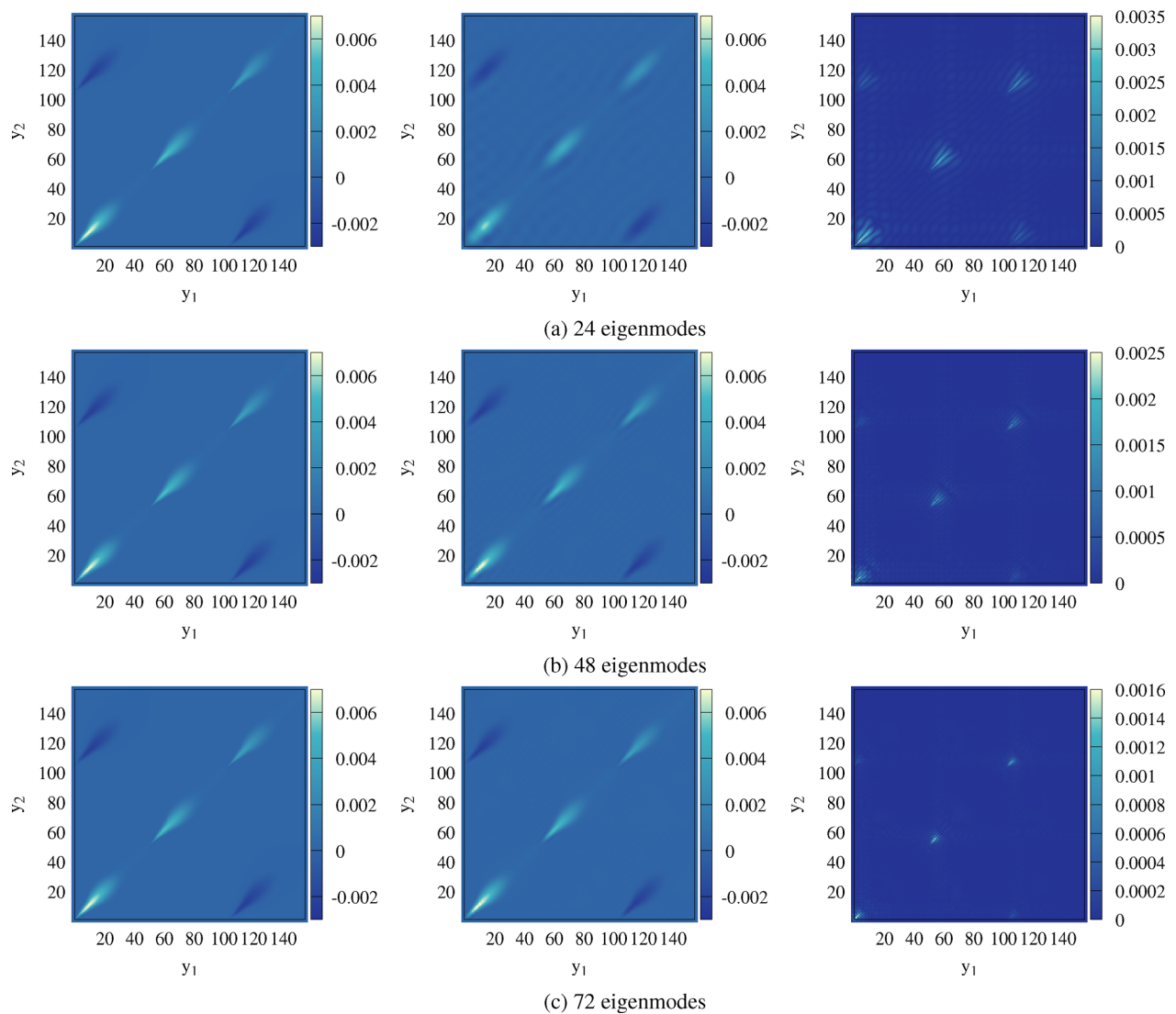


FIG. 2. Reconstructed statistics in two dimensions. [156 × 156 samples are used, three numbers of eigenmodes are shown in (a)–(c). In each group, the left figure is its initial covariance tensor before decomposition, the middle figure shows the covariance with compression, and the right figure shows the error between original and compressed covariance.]

specific in many studies of industrial interest. So, it is expedient to specialize in the decomposition of this type of computational domain. In such cases, the procedure will be simplified. In the direction where the domain is periodic and the correlation is homogeneous, the eigenvectors are sine and cosine functions, and the eigenvalues are corresponding Fourier amplitudes. We can generate the velocity field in the Fourier space.

Let $\tilde{u}_j(y, z)$, $\tilde{v}_j(y, z)$, $\tilde{w}_j(y, z)$ be the velocity components of the j th scaled eigenvector at the position (y, z) . The turbulence intensity in the free stream is indicated in the scaled eigenvectors shown in Eq. (13). The turbulence elements for each wavenumber are taking the form as

$$\begin{bmatrix} \tilde{u}_j(y, z) \\ \tilde{v}_j(y, z) \\ \tilde{w}_j(y, z) \end{bmatrix}_\kappa = \begin{bmatrix} \hat{u}_j(y) \\ \hat{v}_j(y) \\ \hat{w}_j(y) \end{bmatrix} e^{i \frac{2\pi \kappa}{W} z}. \quad (14)$$

In the end, the actual search of eigenvalues and eigenvectors is only necessary in the non-homogeneous directions. Once the correlation function is known from the preliminary simulation, the 3D reconstruction problem reduces to a 1D eigenvalue problem and a computation of matrix-vector product.

3. Wave number space

The energy spectrum is described by the discrete signal $[\tilde{u}_{jk}(y, z), \tilde{v}_{jk}(y, z), \tilde{w}_{jk}(y, z)]^T$ in the wavenumber space. If energy is equally distributed over the wavenumber range, the turbulence generated will decay immediately and flow will laminarize because the signal is white noise. A realistic energy spectrum is therefore needed. The spectrum of turbulence is universal.

If the total turbulent energy of the spectrum matches the turbulent energy from the preliminary simulation, the discrete wavenumber amplitude can be distributed with an energy spectrum of a suitable shape. An approximate spectrum is proposed as

$$f_\kappa = \frac{1}{F} \begin{cases} \left(\frac{\kappa}{N_I}\right)^4, & \kappa \leq N_I, \\ \left(\frac{\kappa}{N_I}\right)^{-5/3}, & \kappa > N_I, \end{cases} \quad (15)$$

$$F = \left(\sum_{\kappa=1, N_I} \left(\frac{\kappa}{N_I}\right)^4 + \sum_{\kappa=N_I+1, N} \left(\frac{\kappa}{N_I}\right)^{-5/3} \right). \quad (16)$$

A more simplified model is reasonable from observations

$$f_\kappa = \frac{1}{F} \begin{cases} 1, & \kappa \leq N_I, \\ \left(\frac{\kappa}{N_I}\right)^{-5/3}, & \kappa > N_I, \end{cases} \quad (17)$$

$$F = \left(\sum_{\kappa=1, N_I} 1 + \sum_{\kappa=N_I+1, N} \left(\frac{\kappa}{N_I}\right)^{-5/3} \right). \quad (18)$$

The shape of the spectrum above is suggested by the inspection of turbulence spectra in boundary layers reported in the literature (see, e.g., Klebanoff³⁹). The dividing wavenumber N_I corresponds to the wavelength that is comparable to the momentum thickness, shown in

Eq. (19). Here, a control parameter α_I is introduced to make the shape of the spectrum adjustable, which will be discussed in the results

$$N_I = \frac{W}{\alpha_I \theta}. \quad (19)$$

Thus, for a discrete signal on the point of wall-normal coordinate y and spanwise coordinate z , a two-dimensionally decomposed mode can be constructed as

$$\begin{bmatrix} \tilde{u}_{jk}(y, z) \\ \tilde{v}_{jk}(y, z) \\ \tilde{w}_{jk}(y, z) \end{bmatrix} = f_\kappa \begin{bmatrix} \hat{u}_j(y) \\ \hat{v}_j(y) \\ \hat{w}_j(y) \end{bmatrix} e^{i \frac{2\pi \kappa}{W} z}, \quad (20)$$

where j is the eigenmode index, which represents the decomposition in the wall-normal direction, and k is the Fourier mode index, which represents the decomposition in the spanwise direction.

4. Correlated random sequence generation

In Sec. II D 3, a signal that displays the desired second-order statistics in space has been constructed. We now introduce a correlated random factor $s_{jk}(t)$ to make

$$\begin{bmatrix} u' \\ v' \\ w' \end{bmatrix}(y, z, t) = s_{jk}(t) \begin{bmatrix} \tilde{u}_{jk} \\ \tilde{v}_{jk} \\ \tilde{w}_{jk} \end{bmatrix}(y, z), \quad (21)$$

a signal that displays the desired second-order statistics in time as well.

Equation (21) presents a turbulence signal containing the Reynolds stresses information, so there is no need to operate “decoupling” as in other precursor-synthesizing methods. The term decoupling denotes a linear transformation that takes place after length scales are imposed on individual velocity components. Decoupling takes place via a tensor³⁰ that makes independent velocity fluctuations to match a desired Reynolds stress tensor. Fathali⁴⁰ showed that decoupling causes simulated length scales to deviate from their prescribed values.

5. The digital time filter

$s_{jk}(t)$ can be formed from an uncorrelated sequence. This task can be accomplished by a filtering method. The original filter-based^{33,41,42} signal synthesizing is in nature a linear combination, the linear coefficients of which determine the two-time correlations. These correlations are either constructed from a given Gaussian shape³³ or from a detailed derivation.⁴¹ The resulting velocities can reproduce first- and second-order one-point statistics as well as two-point correlations. These filter-based methods have built synthetically correlated turbulence that matches well with isotropic data.

A signal for a time node by convolution is to be associated with the current time point, the past, and the future. Here, a new digital filter is proposed. The digital filter for a mode jk is constructed as

$$\psi_{jkl} = e^{-\left(\frac{\Delta t}{\tau_{jk}}\right)^2}, \quad (22)$$

where τ_{jk} is a timescale associated with mode jk , Δt the time separation that corresponds to two consecutive samples, and l is a time index.

The subscript l varies between $-M_t$ and M_t , where M_t is the time filter support. We thus have two questions: (i) How to define the timescale τ_{jk} ? (ii) How do we find a reasonable time filter support M_t ? The second question is discussed in Sec. IV B 2.

The first question is solved based on the consideration of a temporal simulation. Taylor's hypothesis is a useful tool for relating spatial and temporal data via a convection velocity. The validity of Taylor's hypothesis has been proved by Lee²⁶ when the turbulence level is low, viscous forces can be ignored and the mean shear is not large. Wills⁴³ studied different convection velocities for turbulent fluctuations in the shear layer. In Lee's incompressible condition, the convective velocity has been shown nearly the same as the mean flow velocity except for very small eddies. In this study, these observations are exploited for using Taylor's hypothesis: the timescale of turbulence structures dominated by a certain mode from the inflow slice is transformed from the corresponding spatial scale via the mean freestream velocity (considered reasonable as the convective velocity), for a simplified expression

$$\tau_{jk} \approx W/U_0 \kappa, \quad (23)$$

where τ_{jk} is a timescale associated with mode jk . This simplified timescale assigns the same timescale to a mode regardless of wall-normal length scales. To avoid this drawback, the variation of velocity along the transverse direction (normal to the wall) should be included. This can be accomplished by the following expression:

$$\tau_{jk} = \frac{1}{U_0} \left(\frac{\alpha}{\int_0^{y_{\max}} \left(\frac{du}{dy} \right)_j^2 dy} + \beta \frac{W^2}{\kappa^2} \right)^{1/2}, \quad (24)$$

where coefficients α and β are taken as 1. The results shown in this study are all applied with the latter timescale formulation.

Once the τ_{jk} is obtained, an uncorrelated random sequence $r_{jkl}(t)$ can be built to make the correlated sequence $s_{jk}(t)$. This can be accomplished through the convolution

$$s_{jk}(t) = r_{jkl}(t) \psi_{jkl}. \quad (25)$$

Finally, after summing over all possible values of κ and j , a random velocity field will result with the covariance tensor equal to the one we started from.

A random correlated (y - z) velocity field can be generated by

$$\begin{bmatrix} u'(y, z, t) \\ v'(y, z, t) \\ w'(y, z, t) \end{bmatrix} = \sum_{l=-M_t/2}^{M_t/2} \sum_{\kappa=-N, \kappa \neq 0}^N \sum_{j=1}^m r_{ljk}(t) \begin{bmatrix} \hat{u}_j(y) \\ \hat{v}_j(y) \\ \hat{w}_j(y) \end{bmatrix} f_{\kappa} e^{i \frac{2\pi \kappa}{W} z} \psi_{jkl}, \quad (26)$$

where r_{jkl} is a random complex variable with ($*$ denotes complex conjugate)

$$r_{jkl} = r_{j(-\kappa)l}^*. \quad (27)$$

The integer κ goes from $-N$ to N . N is chosen to represent the number of spanwise Fourier harmonics. If there are 128 cells in the spanwise direction, N could be 32.

III. NUMERICAL TECHNIQUE

A. LES flow solver

The LES simulations are performed by solving the Navier–Stokes equations by a homegrown CFD code “H4X.” The code adopts an implicit LES based on the finite volume approach. The spatial derivatives at the interior points are solved by a third-order scheme that utilizes a non-linear limiter based on a compact three-point stencil. This scheme can well handle discontinuities as well as local extrema while maintaining the diffusion error as low in the smooth region. The mesh is generated by a built-in meshing generator.⁴⁴ Different time discretization options are provided according to the application. The implicit dual time stepping method is adopted in low Reynolds number situations, while the explicit Runge–Kutta method is adopted in medium Reynolds number situations.

B. Inflow generator implementation

As shown in Fig. 3, the whole procedure is separated into the pre-simulation section and the main simulation section. Given the basic information about mean flow, the preprocessing guesses a covariance tensor, builds eigenvectors and digital filters, and interpolates modes onto the target cloud of grid points on the inlet slice of the computational domain. The mean velocity profiles, the modes, and corresponding coefficients on the cell center of the required points are prepared before the LES simulation. The whole preprocessing can be finished within seconds and is needed only once for one case. The final

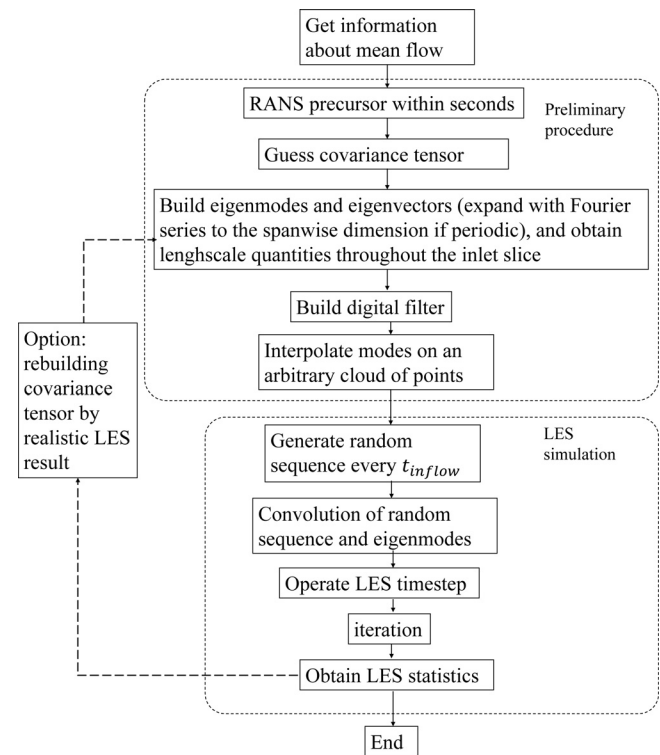


FIG. 3. The whole procedure of an LES simulation with inflow generator.

velocity signal is then reconstructed from those prepared modes weighted by corresponding coefficients according to

$$\begin{bmatrix} u(y, z, t) \\ v(y, z, t) \\ w(y, z, t) \end{bmatrix} = \begin{bmatrix} \bar{u}(y, z) \\ \bar{v}(y, z) \\ \bar{w}(y, z) \end{bmatrix} + \begin{bmatrix} u'(y, z, t) \\ v'(y, z, t) \\ w'(y, z, t) \end{bmatrix}. \quad (28)$$

The timescale of the inflow signal might be much larger than the numerical time step. As a result, it is not necessary to generate a new inflow field every numerical time step using Eq. (28). For this purpose, a timescale is introduced dt_{inflow} , which is defined as

$$dt_{\text{inflow}} = \frac{\alpha_t \theta}{u M_t}, \quad (29)$$

where α_t is a constant of order 1. Equation (29) is based on Taylor's hypothesis with θ/u as an integral timescale. The number of simulation timesteps between two consecutive updates of the inflow field is dt_{inflow}/dt . Between two consecutive "inflow time steps," the inflow field is obtained by linear interpolating from inflow fields at two neighboring inflow time steps.

IV. APPLICATION FOR A CHANNEL

One of the simplest wall-bounded turbulent flows to test is a plane channel. A case with available data published is $Re_\tau = 395$ ($Re_\tau = \delta u_\tau / \mu$). This study shows an LES simulation of the turbulent flow in a three-dimensional channel at $Re_\tau = 395$ by different methods. The LES result is compared with the DNS results from Lee and Moser.⁴⁵

The computational domain has the dimensions of $10\pi\delta$, 2δ , and $\pi\delta$ in the streamwise, wall-normal, and spanwise directions, where δ is the channel half height. The mesh resolution has $x^+ = 20$, $z^+ = 6$, and $y^+ = 0.15$ at the wall and $y^+ = 6$ further away from the wall. The mesh adopts Pirozzoli and Orlandi's⁴⁶ grid stretching method in the wall-normal direction. This stretching method builds mesh by blending close to constant spacing in the viscous layer and spacing proportional to the Kolmogorov length scale in the log layer. Their optimal values of a blending parameter and the near-wall grid spacing are employed to maximize the allowed time step. This meshing procedure guarantees the accuracy and efficiency of computational results. Periodic boundaries are applied in the spanwise direction. The dual time stepping is adopted for time advancing in these LES simulations. The physical time step is set as a quarter of viscous timescale, that is, $\Delta t = 0.25\mu/(u_\tau^2)$, according to Choi and Moin.⁴⁷ The inner iteration of the dual-time scheme applies a third-order four-stage Runge-Kutta scheme. The simulations were initially run for 10 flow-through times to remove the transient effect. Statistics are collected for 14 flow-through times. Both the averaging in the spanwise direction and the mirror averaging along the wall-normal direction are performed at each streamwise position to pursue the convergence of statistics.

A reference simulation (PER0) was performed to compare with all other cases. PER0 is simulated using streamwise periodic boundaries. Its flow is driven by a pressure gradient that is adjusted automatically to maintain a constant mass flux. All the other simulations (INFL0-INFL7) are using the proposed synthetic inflow generator, with different turbulence parameters specified. All the channel simulations adopt the same mesh and numerical schemes. The configurations of channel simulations are summarized in Table I.

TABLE I. Simulations for turbulent channel flow cases at $Re_\tau = 395$.

Cases	Method	Details
DNS0	DNS, periodic calculation	Lee and Moser ⁴⁵
PER0	LES, streamwise periodic boundary	...
INFL0	LES, inflow generator	$\alpha_I = 0.6$, $M_t = 2048$
INFL1	LES, inflow generator	$\alpha_I = 0.75$, $M_t = 2048$
INFL2	LES, inflow generator	$\alpha_I = 1.0$, $M_t = 2048$
INFL3	LES, inflow generator	$\alpha_I = 2.0$, $M_t = 2048$
INFL4	LES, inflow generator	$\alpha_I = 0.75$, $M_t = 1024$
INFL5	LES, inflow generator	$\alpha_I = 0.75$, $M_t = 4096$
INFL6	LES, inflow generator	$\alpha_I = 0.75$, $M_t = 512$
INFL7	LES, inflow generator	$\alpha_I = 0.2$, $M_t = 2048$

A. Validation

The time-averaged mean velocity profiles in wall units at $x/\delta = 15$ are presented in Fig. 4. The profiles closely agree with the logarithmic law $U^+ = 1/k_l \log(y^+) + C$, where $k_l = 0.4$ and $C = 5.5$, starting at $y^+ \approx 20$. Compared with the result from the periodic method and the results from the inflow generator method, the inflow generator method case (INFL0) shows a slight advantage over the case using the periodic method (PER0) in matching the DNS curve in the log-law region. Therefore, the proposed synthetic inflow generator is capable of generating a realistic turbulent velocity profile.

Figure 5 compares the LES result with Lee and Moser's DNS result in terms of the rms of the Reynolds normal stresses ($\langle u'u' \rangle$, $\langle v'v' \rangle$, and $\langle w'w' \rangle$) in wall units. The computed Reynolds normal stresses of both PER0 and INFL0 match well with the DNS result. The slight underpredicting of w'^+ near $y^+ = 40$ is shown in both PER0 and INFL0. This underpredicting is presumably caused by the numerical scheme in the LES code. Both the v'^+ of INFL0 and the v'^+ of PER0 nearly overlap the corresponding DNS curve. The u'^+ of INFL0 becomes overpredicted when $y^+ > 80$. The u'^+ of INFL0 in the $y^+ < 80$ region and the u'^+ of PER0 throughout all the y^+ regions agree well with the counterpart DNS results. The errors mentioned above are acceptable. The error

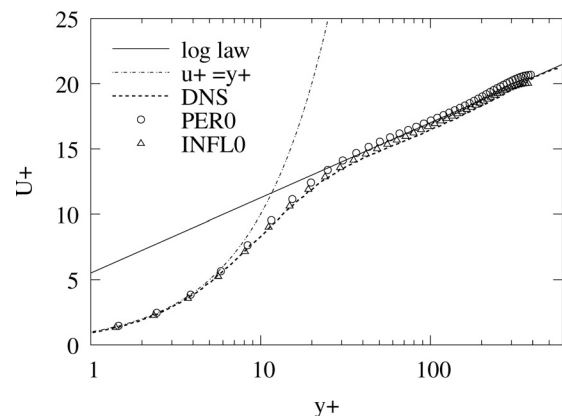


FIG. 4. Mean velocity profiles for a $Re_\tau = 395$ channel at $x/\delta = 15$. Results are compared with the log law $U^+ = 1/k * \log(y^+) + C$ and DNS results.⁴⁵

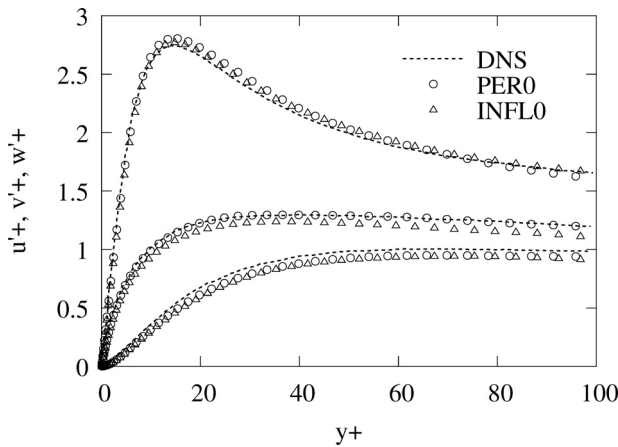


FIG. 5. Rms velocity profiles in wall coordinates for a $Re_\tau = 395$ channel at $x/\delta = 15$. LES results are compared with DNS results.⁴⁵ The curves with the amplitudes from high to low are u^+ , w^+ , and v^+ .

can be minimized when the energy spectrum, the time filter support, and the t_{inflow} are specified as optimum. The effect of these parameters on the shape of velocities and turbulence intensities will be discussed in Sec. IV B.

B. Turbulence parameters

1. The effect of the specified energy spectrum

The shape of the specified energy spectrum is decided by controlling α_I in Eq. (19). A larger α_I means that the inertial region starts from a smaller wavenumber in the approximate spectrum, and leaves a wider inertial region, as indicated by the energy spectrum shown in Fig. 6.

The prescribed energy spectrum is evaluated by the development of velocity profiles and turbulence intensities downstream of the inlet, shown in Figs. 7 and 8. The solid line represents the reference case PER0. INFL0, INFL1, INFL2, INFL3, and INFL7 are cases using the inflow generator prescribed with α_I between 0.2 and 2.

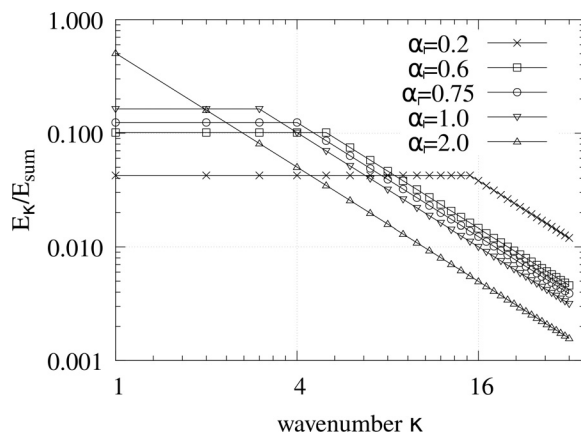


FIG. 6. Energy distribution along wavenumber by different partitions.

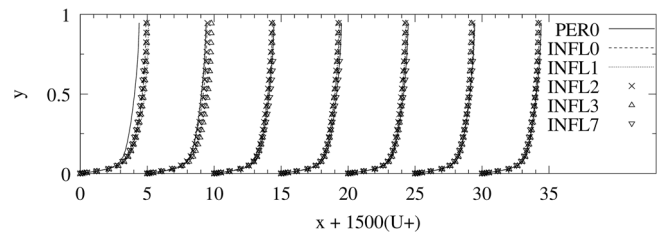


FIG. 7. Downstream development of the velocity profiles downstream the inlet on the bottom half of channel.

Figure 8 shows the Reynolds normal stresses and the Reynolds shear stress along the streamwise direction. In Fig. 8, INFL3 and INFL7 require the longest development length. This is due to either a too large α_I (INFL3) or a too small α_I (INFL7). INFL3 requires 20δ for the development length of u^+ . Although u^+ and w^+ are not very different in between INFL3 and PER0 at 10δ downstream from the inlet, the v^+ of INFL3 in the near-centerline region maintains a deviation from the PER0 counterpart until the outlet. In contrast, in INFL0, INFL1, and INFL2, u^+ , v^+ , w^+ , and $u'v'$ collapse onto their counterparts in PER0 from around $x/\delta = 10$.

Above all, INFL2 is the one that collapses onto PER0 most rapidly and that is the closest to PER0. INFL1 and INFL0 are also acceptable. This means that the optimum starting position of the inertial region on the approximate spectrum is when $0.6 < \alpha_I < 1$ ($\alpha_I = 1$ is the best) in this case. The error of INFL3 also indicates that an approximate flat infrared region is needed as a part of the spectrum: ignoring the flat infrared region may result in overpredicted Reynolds normal stresses and Reynolds shear stress. On the contrary, if the wavenumber at the start of the inertial region is set too large, Reynolds normal stresses and the Reynolds shear stress will be underpredicted. This is because when little energy is allocated to lower wavenumbers on the spectrum, small turbulence structures are destroyed immediately.

Figure 7 shows the development of the velocity profiles downstream from the inlet. It shows that the velocity profiles of all inflow cases collapse onto PER0 downstream from $x/\delta = 10$. Adjusting the intersection point on the energy spectrum does not make much difference to the velocity profiles downstream from the end of the inlet development section, which is of 10δ in this channel case.

2. The effect of the specified time filter

In the proposed time filtering method, the shape of the time integration can be decided by adjusting the frequency of time sampling and the total number of physical time samples, namely, the time filter control parameter α_t and the time filter support M_t . To guarantee that all energy-containing modes can be presented, inflow time samples should be sufficient and reasonably distributed. For this purpose, an optimum ratio of M_t to α_t is first searched for to select the number of inflow generator time samples. Fixing the ratio of M_t to α_t , the shape of the time filtering is then controlled by only adjusting M_t , as indicated in Eq. (29). Figure 9 shows the time filtering for different combinations of M_t and α_t . Figures 9(a), 9(c), and 9(e) show that when the ratio of M_t to α_t is too large, the time samples of lower index modes may become truncated, thus leading to incomplete total kinetic energy. By contrast, when the ratio of M_t to α_t is too small, there may be not

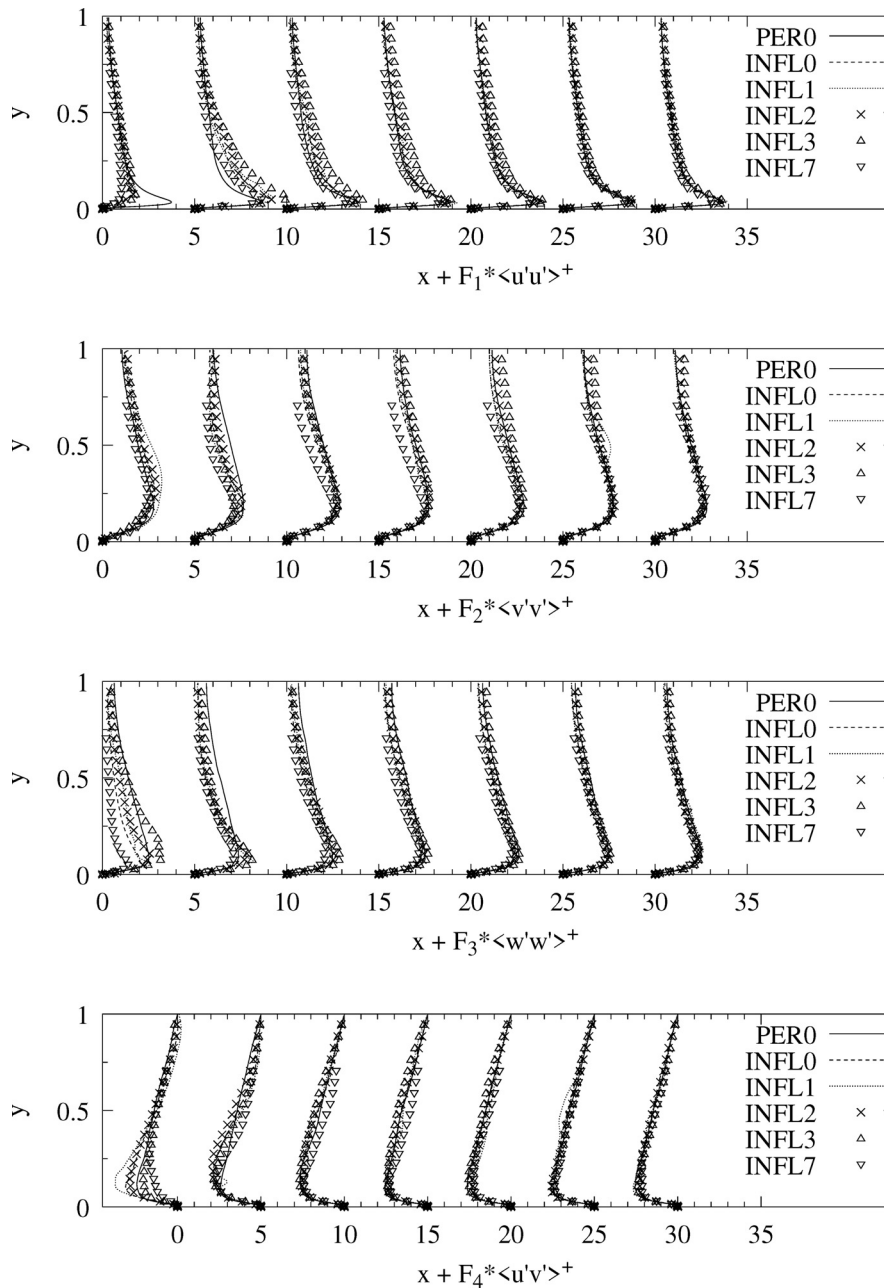


FIG. 8. Downstream development of the normal stress and Reynolds stress downstream the inlet on the bottom half of channel. From top to below are $(x + F_1 * u^+, x + F_2 * w^+, x + F_3 * v^+, x + F_4 * uv^+)$, where F_1, F_2, F_3 , and F_4 are scaling factors).

enough sample points to sketch the highest modes. Figures 9(a), 9(b), and 9(f), or 9(c) and 9(d) show that when the ratio of M_t to α_t is same, indicating a same inflow time step dt_{inflow} , a larger M_t results in a more concentrated time distribution, while the peak amplitude of each corresponding mode is kept the same. For $M_t/\alpha_t = 64$, $M_t = 512$ leads to an incomplete “Gaussian shape” of the time distribution of the lower index mode, while $M_t = 2048$ leads to an over-concentrated time distribution of all of modes. For $M_t/\alpha_t = 32$, $M_t = 1024$, all of modes are expressed with sufficient sample points when $M_t > 512$.

Figures 9(d)–9(f) show that the tightness of the time samples of each mode is dependent on α_t . Given a same $\alpha_t = 32$, $M_t < 1024$ may not provide enough samples for the peak of the highest modes. As a result, 32 is chosen as an optimum ratio of M_t to α_t and is used in all the cases shown below.

Figure 10 shows the development of the Reynolds normal stresses and the Reynolds shear stress downstream from the inlet. It compares the inflow generator cases by using different time filter supports with the reference case PER0. Since the M_t and α_t that may cause

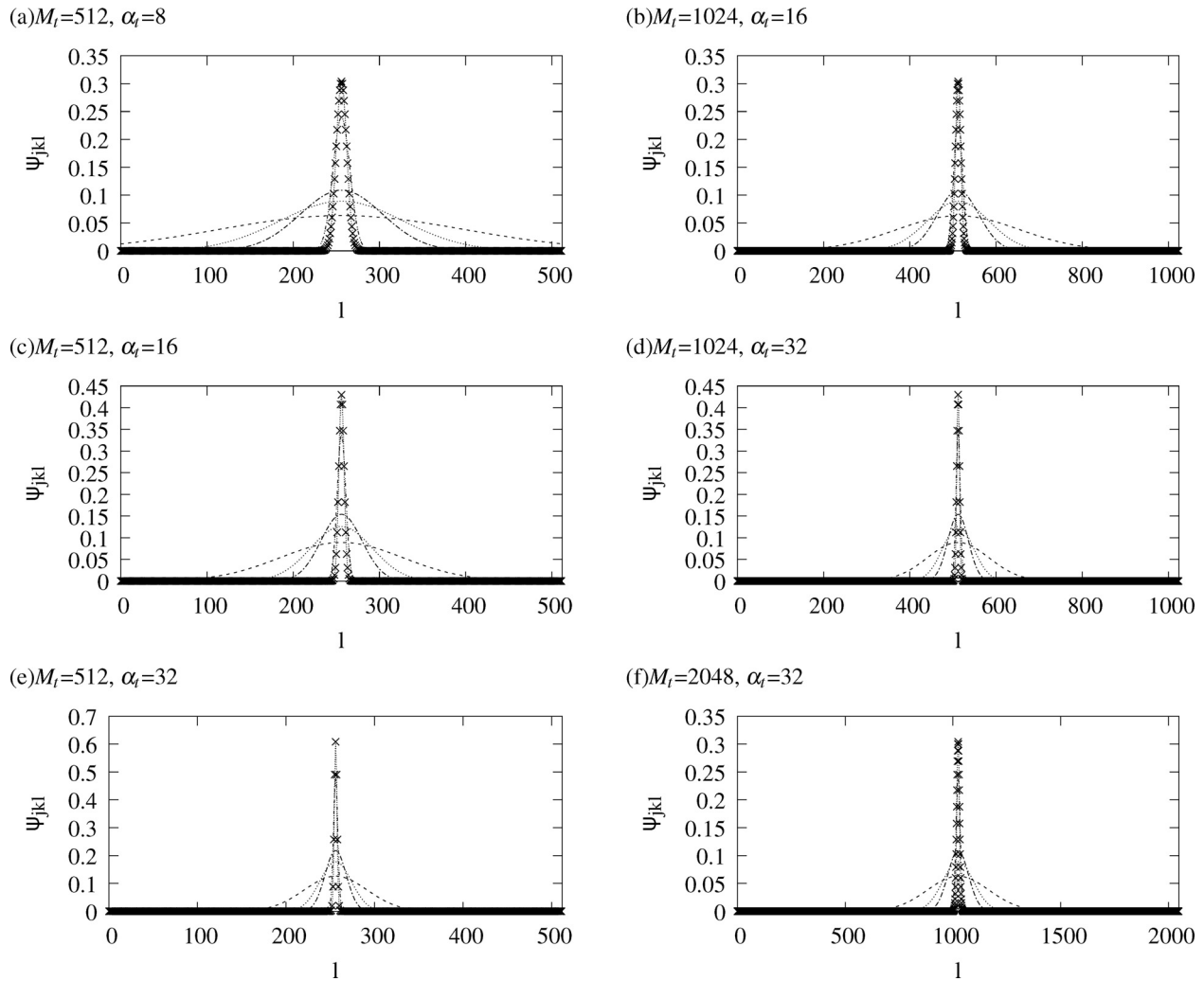


FIG. 9. Time distribution of modes with different Fourier index in the first eigenmode [dash line: first Fourier mode, dot line: second Fourier mode, dash dot line: third Fourier mode, dash dot line: 16th Fourier mode, dot line with cross symbols: 32th Fourier mode; (a) $M_t = 512$, $\alpha_t = 8$; (b) $M_t = 1024$, $\alpha_t = 16$; (c) $M_t = 512$, $\alpha_t = 16$; (d) $M_t = 1024$, $\alpha_t = 32$; (e) $M_t = 512$, $\alpha_t = 32$; and (f) $M_t = 2048$, $\alpha_t = 32$].

incomplete Gaussian shape of modes have been excluded in advance, the considered values for the time filter support M_t makes little difference to the turbulence intensities. This suggests that $M_t = 1024$ is already sufficient for the simulated case. On the other hand, further increasing the time samples beyond this value will not help fasten the collapse or shorten the inlet development length.

Figure 11 shows the development of the scaled Reynolds shear stress downstream from the inlet. The proposed synthetic inflow generator is compared with Batten's method⁶ and Jarrin's synthetic-eddy inlet condition (SEM).⁷ INFL4, INFL5, and INFL6 are not shown here as their patterns are similar to INFL1 according to Fig. 10.

Among the six situations shown in Fig. 11, the Reynolds shear stress prescribed by Batten's method decays most significantly before being regenerated slowly when going downstream from the inlet. It ends up with non-negligible errors localized around the channel mid-height.

Jarrin⁸ attributed this error to "an overly large timescale of the inflow data." On the contrary, the synthetic inflow generator proposed in this study and Jarrin's SEM method⁸ present Reynolds shear stress profiles that rapidly collapse onto the realistic reference (represented by PER00) profiles after a small transient. Among the considered situations, INFL0 has the smallest "transient": the levels of Reynolds shear stress agree well with PER0 in the core of the channel and the near-wall region at $x = 5\delta$, while they agree well in the log law region at $x = 10\delta$. INFL1 and INFL2 also have shorter transient than SEM: 5δ in the core of the channel and in the near-wall region; less than 15δ in the log law region. INFL3 has a longer transient than INFL0, INFL1, or INFL2 due to the less realistic energy spectrum of INFL3. This is caused by a too high α_t for INFL3, which leads to a lack of coherence in the turbulent flow. Despite this, the Reynolds stress of INFL3 is on the same level as the SEM result counterparts. This also suggests that if using the synthetic

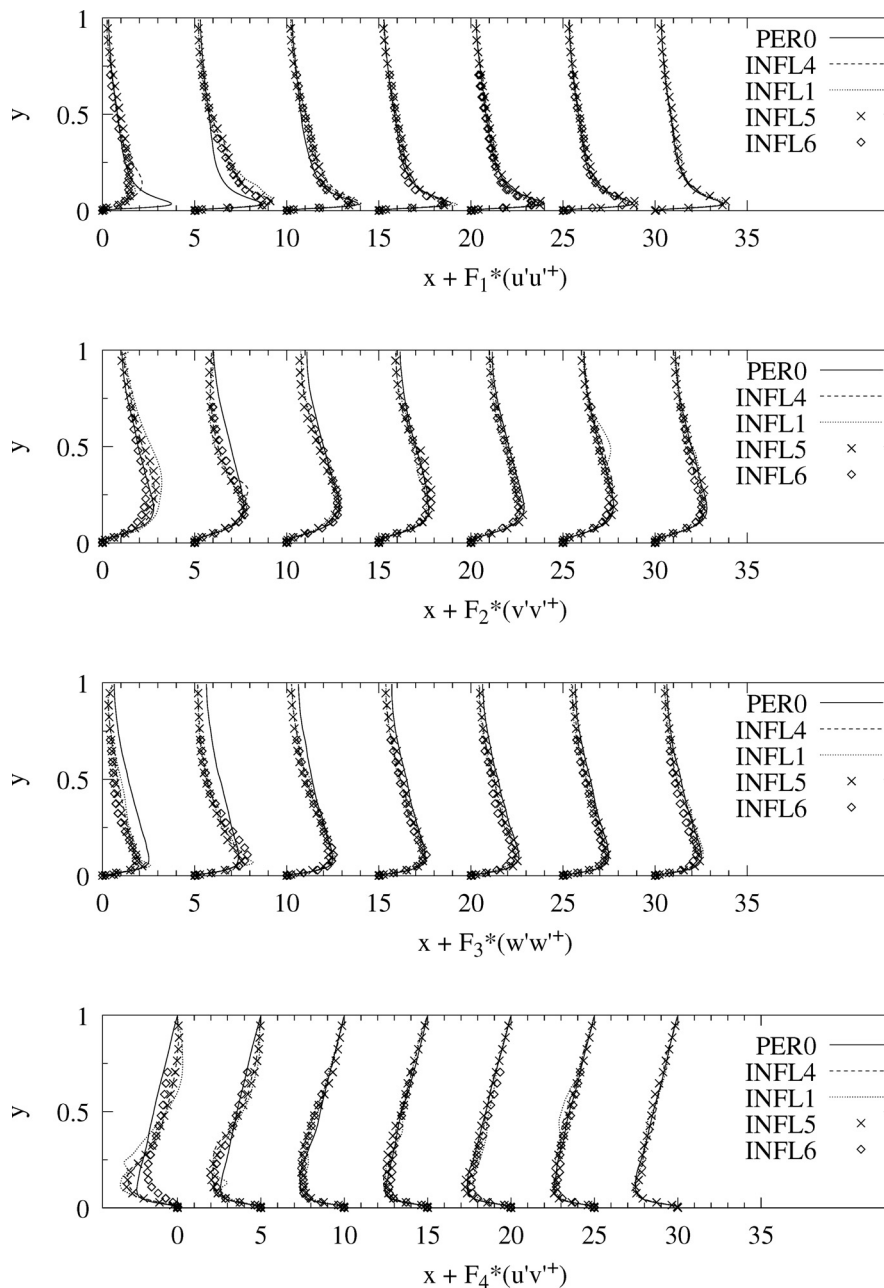


FIG. 10. The development of the normal stress and Reynolds stress downstream from the inlet on the bottom half of channel.

inflow generator proposed in this study, it is still possible to obtain a realistic turbulent inflow by conveniently adjusting the control parameter for the spectrum shape.

In summary, as long as the parameters (M_b , α_l) are correctly chosen, the regeneration of the Reynolds shear stress can quickly match the reference data. Compared with other methods (including Batten's and SEM), the matching of the proposed inflow generator can be more closed and the transient section from the inlet can be shorter. This is mainly because, rather than using uniform length scales for different heights as in other methods, the synthetic inflow generator

specifies realistic length scales for corresponding heights, which are estimated from the preliminary EARSM calculation.

C. Turbulence structures

Figure 12 presents the whole flow field of LES results using the periodic method and the synthetic inflow generator method. These two transient fields present similar turbulence features after a short development length. Similar timescales and length scales can be observed in the corresponding heights of the two results. Figure 13

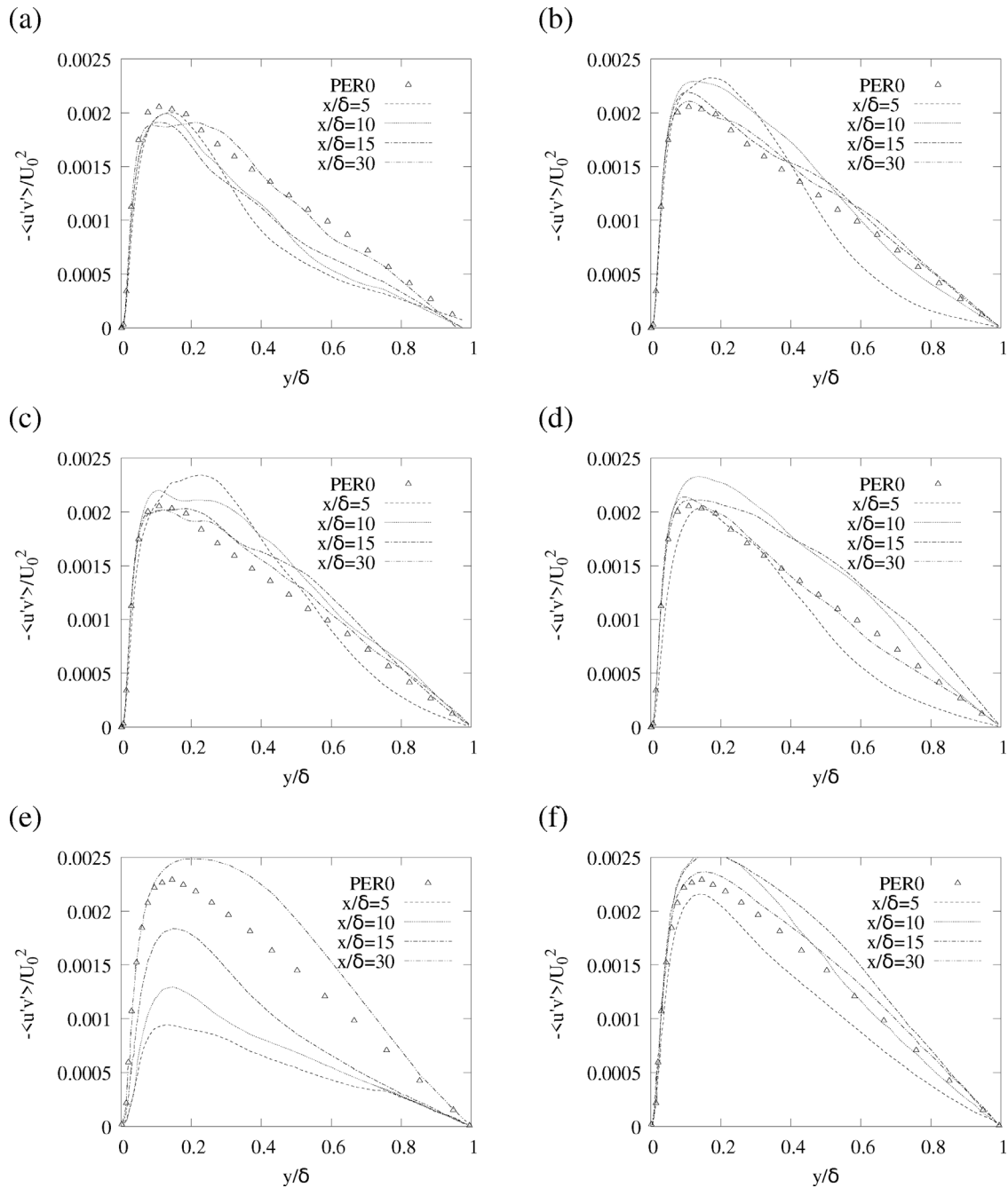


FIG. 11. Profiles of Reynolds shear stress at various streamwise locations in the LES region: (a) INFL7, (b) INFL0, (c) INFL2, (d) INFL3, (e) Batten's method,⁶ and (f) Synthetic-eddy inflow method.⁷ $x/\delta = 5$ (dashed line); $x/\delta = 10$ (dash-dot line); $x/\delta = 15$ (dotted line); $x/\delta = 30$ (solid line); symbols represent periodic LES results. Figures (e) and (f) are reproduced with permission from Jarrin *et al.*, *Int. J. Heat Fluid Flow* **30**, 435–442 (2009) Copyright 2009 Elsevier.

presents their turbulence structures on the $y^+ = 1$ surface by streamwise velocity fluctuations, respectively. The near-wall turbulent streaks are well reproduced in terms of length scales and timescales. Therefore, the proposed synthetic generator has a good capability of reproducing realistic turbulence features in channel flows.

V. APPLICATION FOR A DEVELOPING BOUNDARY LAYER

This section takes a developing boundary layer case as an example to provide general guidance for new users on how to select related parameters for using the proposed synthetic inflow generator.

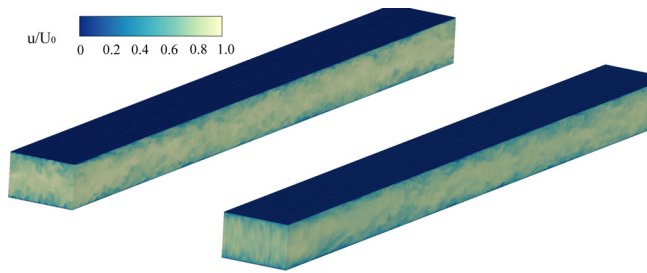


FIG. 12. Downstream development of the velocity profiles downstream from the inlet (3D view, left: PER0, right: INF1).

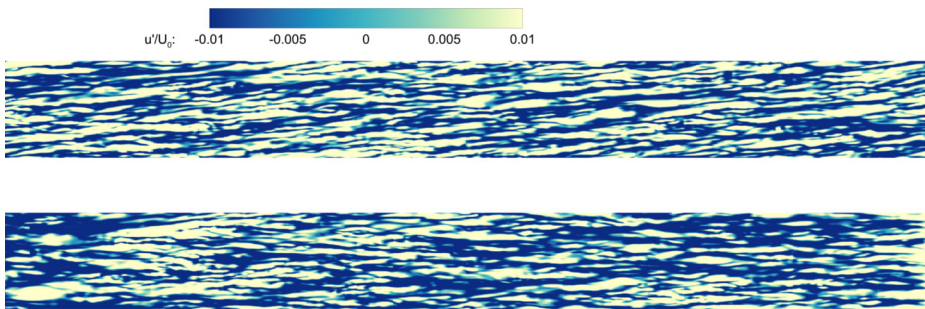


FIG. 13. Downstream development of the velocity profiles downstream from the inlet at the $y^+ = 10$ plane (top: PER0, bottom: INF1).

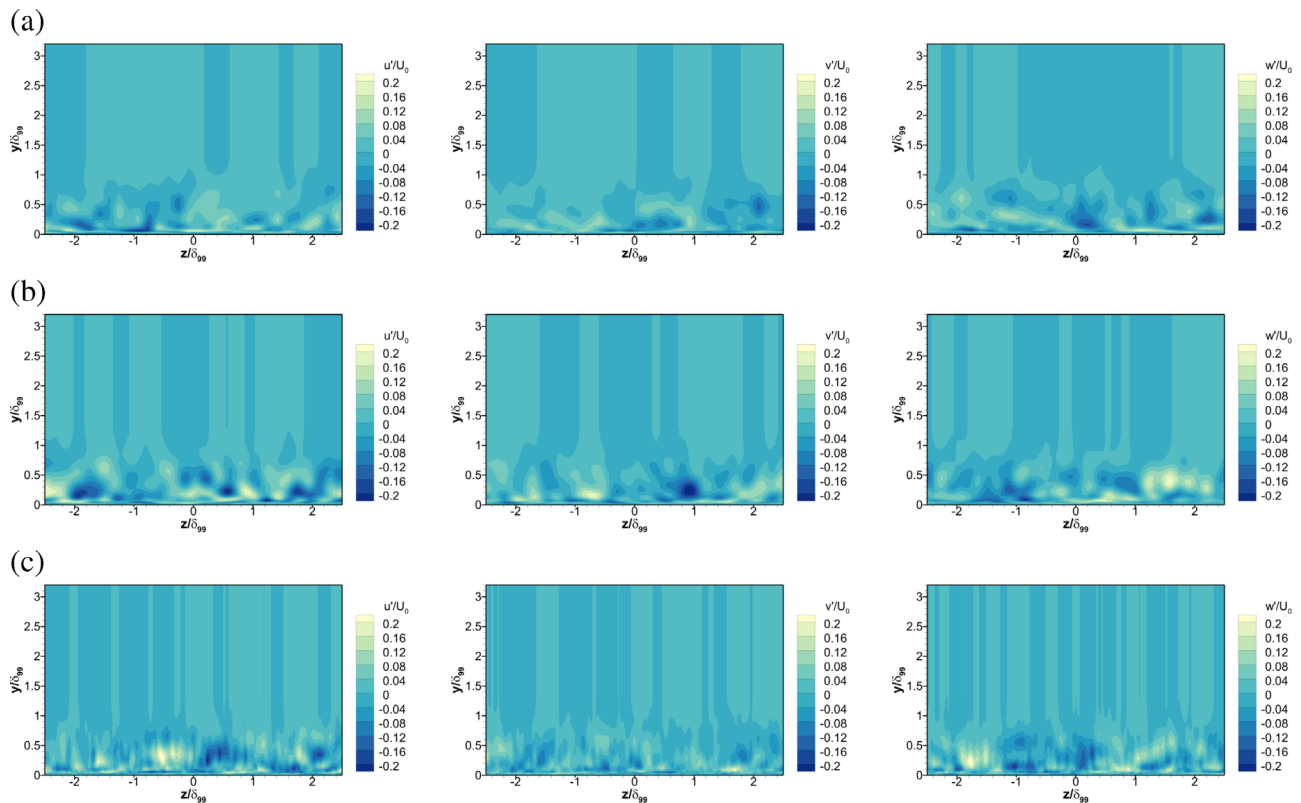


FIG. 14. Turbulence intensities generated at the inflow slice after the same steps: (a) $N_f = 16$, (b) $N_f = 32$, and (c) $N_f = 64$.

The effect of related controlling parameters on the generated inflow is also discussed.

A. Flow configuration

Sparlart's DNS boundary layer at $Re_\theta = 670$ is targeted. A case of a moderate Reynolds number can be the best test case with a complete log layer and more easily observable turbulent features. The domain size is $100\delta^* \times 20\delta^* \times 25\delta^*$. The grid spacing in x , y , and z directions is, in wall units, $\Delta x^+ = 23$, $\Delta y^+ = 0.18$, $\Delta z^+ = 7.8$. The number of points in the y -direction is adjusted to accommodate ten points within 18 wall units. The numbers of cells are $256 \times 168 \times 192$ in three dimensions, with 6 291 456 grids in total. Seven flow-through times

are run to guarantee that the turbulence reaches a statistically steady state, following that statistics are collected for ten flow-through times. Lateral averaging is performed when analyzing statistics at each streamwise location to guarantee the convergence of statistics.

B. Method parameters

The parameters needed to be set up are the number of Fourier modes specified in the spanwise direction N_f , the number of samples for interpolation in the spanwise direction N_z , the time filter support M_p , the α_l which controls the specified spectrum shape and the retained energy ratio.

1. Spanwise modes

If the flow has a homogenous direction, the spatial variation in the spanwise direction can be described in Fourier modes. The number of modes in the Fourier series is N_f . This section examines the effect of N_f on the property of the flow field. Figure 14 shows turbulent

velocities of the generated inflow field on the inlet slice using $N_f = 16$, 32, 64 Fourier modes in the spanwise direction at the same time step with identical values of all other parameters. As shown in Fig. 14, N_f affects the spatial distribution and the strength of turbulent structures.

If the shape of the spectrum is retained, the number of large structures scales approximately with N_f . As an example, approximately four large structures are presented when $N_f = 16$ [shown in Fig. 14(a)], approximately eight large structures are presented when $N_f = 32$ [shown in Fig. 14(b)], and approximately 16 large structures are presented when $N_f = 64$ [shown in Fig. 14(c)]. A larger N_f means an increased size of the part of the spectrum obeying the $-5/3$ curve. As a consequence, as N_f increases, more energy is distributed to the higher waves. Given a value of N_f , multiple coherent turbulence structures are generated next to the wall. The size distribution of these structures depends on N_f . The value of N_f is selected as three to four times the number of large structures in the domain.

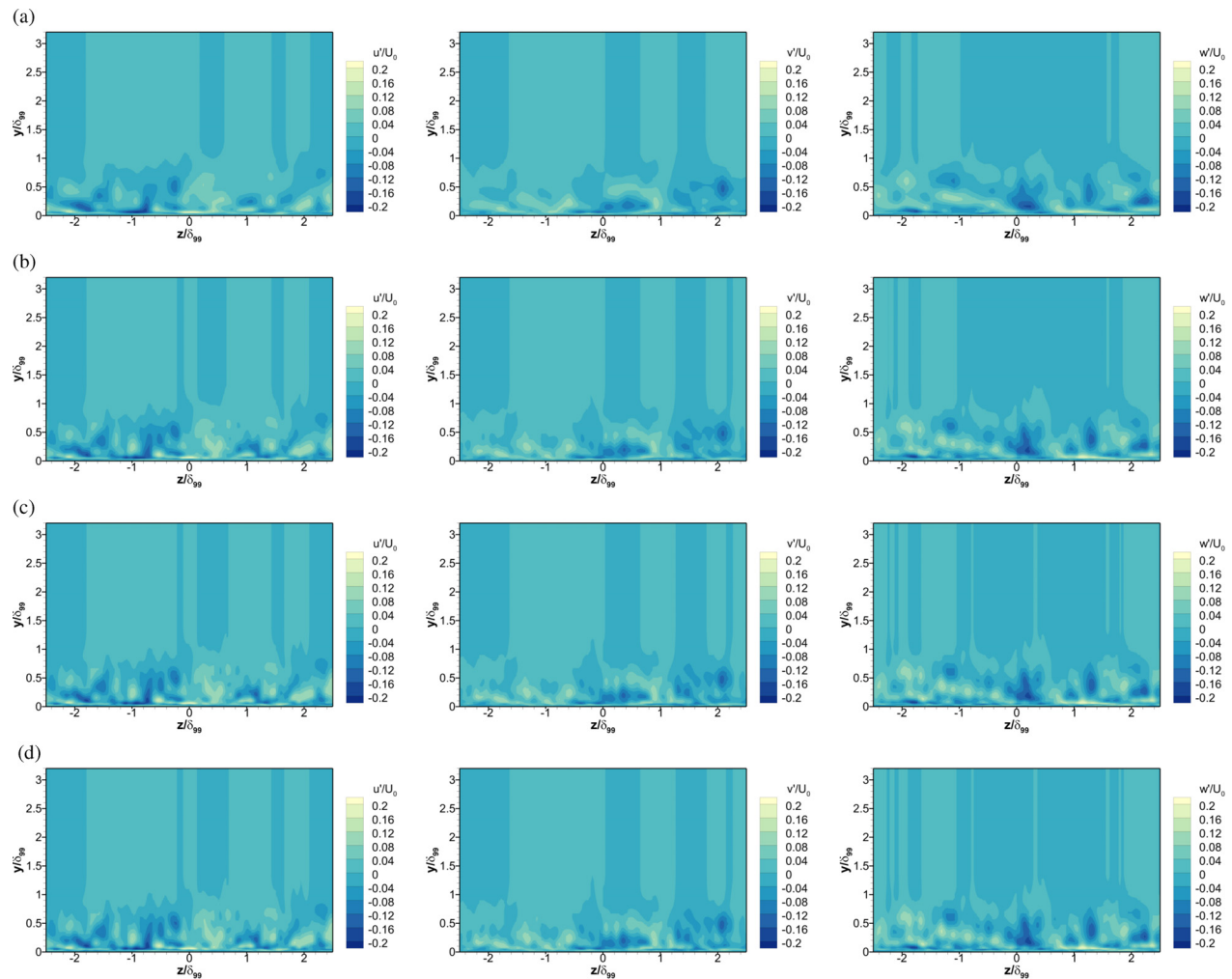


FIG. 15. Turbulence intensities generated at the inflow slice after the same steps: (a) $N_z = 32$, (b) $N_z = 64$, (c) $N_z = 128$, and (d) $N_z = 512$.

N_z is the number of the samples used to reconstruct Fourier modes in the spatial domain for the purpose of interpolation onto the inflow surface. Figure 15 shows turbulent velocities of the generated inflow field on the inlet slice using $N_f = 32$ and $N_z = 32, 64, 128, 512$ interpolation samples in the spanwise direction at the same time step. Using as reference Fig. 15(d), no appreciable difference can be discerned among the cases with $N_z = 512$ [in Fig. 15(d)], $N_z = 128$ [in Fig. 15(c)], and $N_z = 64$ [in Fig. 15(b)]. A loss of resolution can be seen in Fig. 15(a) when $N_z = 32$. In general, the minimum number of samples used for the reconstruction should be $N_z \geq 2N_f$.

2. Time filter

Figure 16 shows the time correlations for the three turbulent velocity components from LES results by using three time filter supports. The correlation coefficient is defined as

$$c(\tau) \equiv \frac{\overline{u_2(t)u_2(t-\tau)}}{u_2^2}. \quad (30)$$

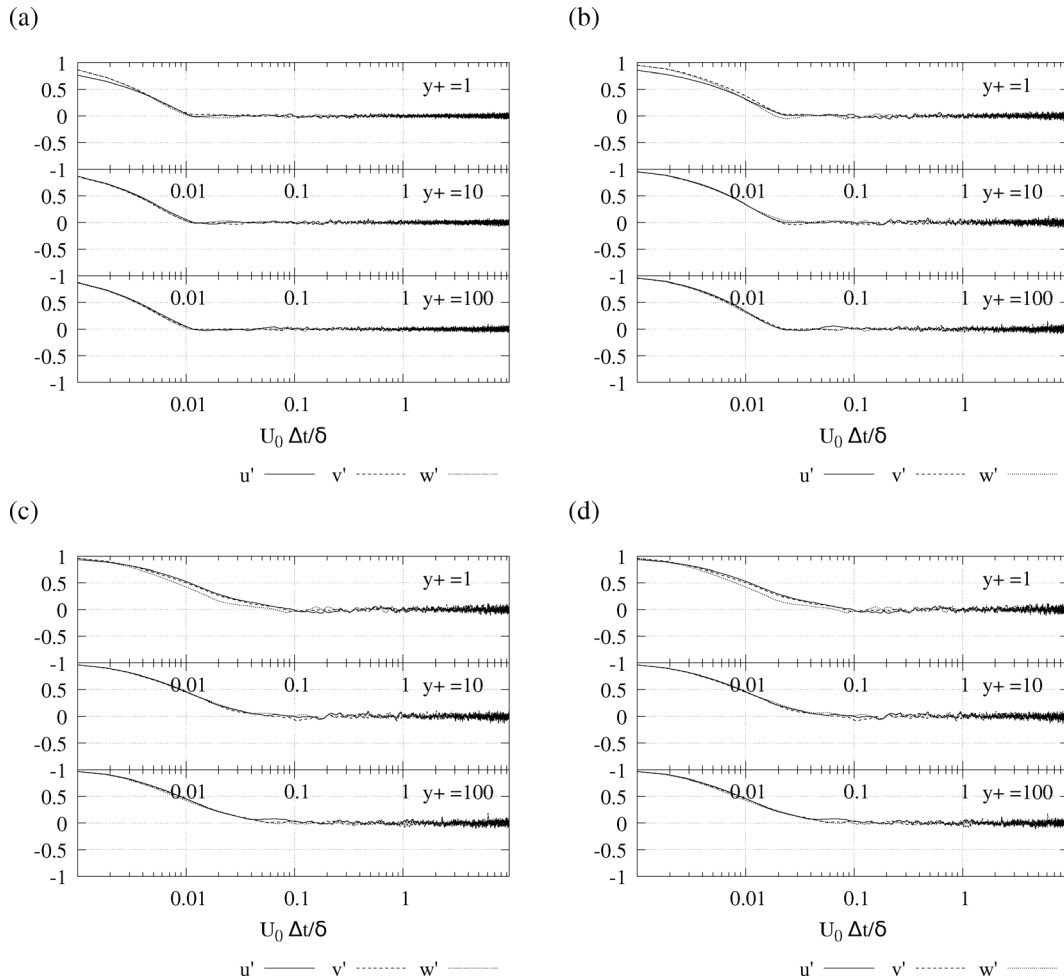


FIG. 16. Time correlations of inflow velocity turbulent components on three y^+ positions: (a) $M_t = 128$, (b) $M_t = 256$, (c) $M_t = 1024$, and (d) $M_t = 2048$.

A larger M_t results in a slower decay of time correlation, whereas a smaller M_t leads to a quicker decay of the time correlation. The integral timescale on a dimensional ground is estimated as proportional to δ/U . The time filter support that results in a decay time longer than the estimated integral length scale is chosen. As a result, $M_t \geq \delta/(U\Delta t)$ is considered sufficient. In this case, $\delta/(U\Delta t) \approx 1024$.

3. Spectrum shape

Two general approaches to spectrum construction are studied, shown in Fig. 17(a): first, a flat line that represents the infrared region is combined with a $-5/3$ power law curve that represents the inertial region; second, a 4 power law curve that represents the infrared region is combined with a $-5/3$ power law curve that represents the inertial region. Once the spectrum construction approach is determined, the shape of the specified energy spectrum is decided by controlling α_I in Eq. (19). A larger α_I means that the inertial region starts from a smaller wavenumber in the approximated spectrum, and leaves a wider

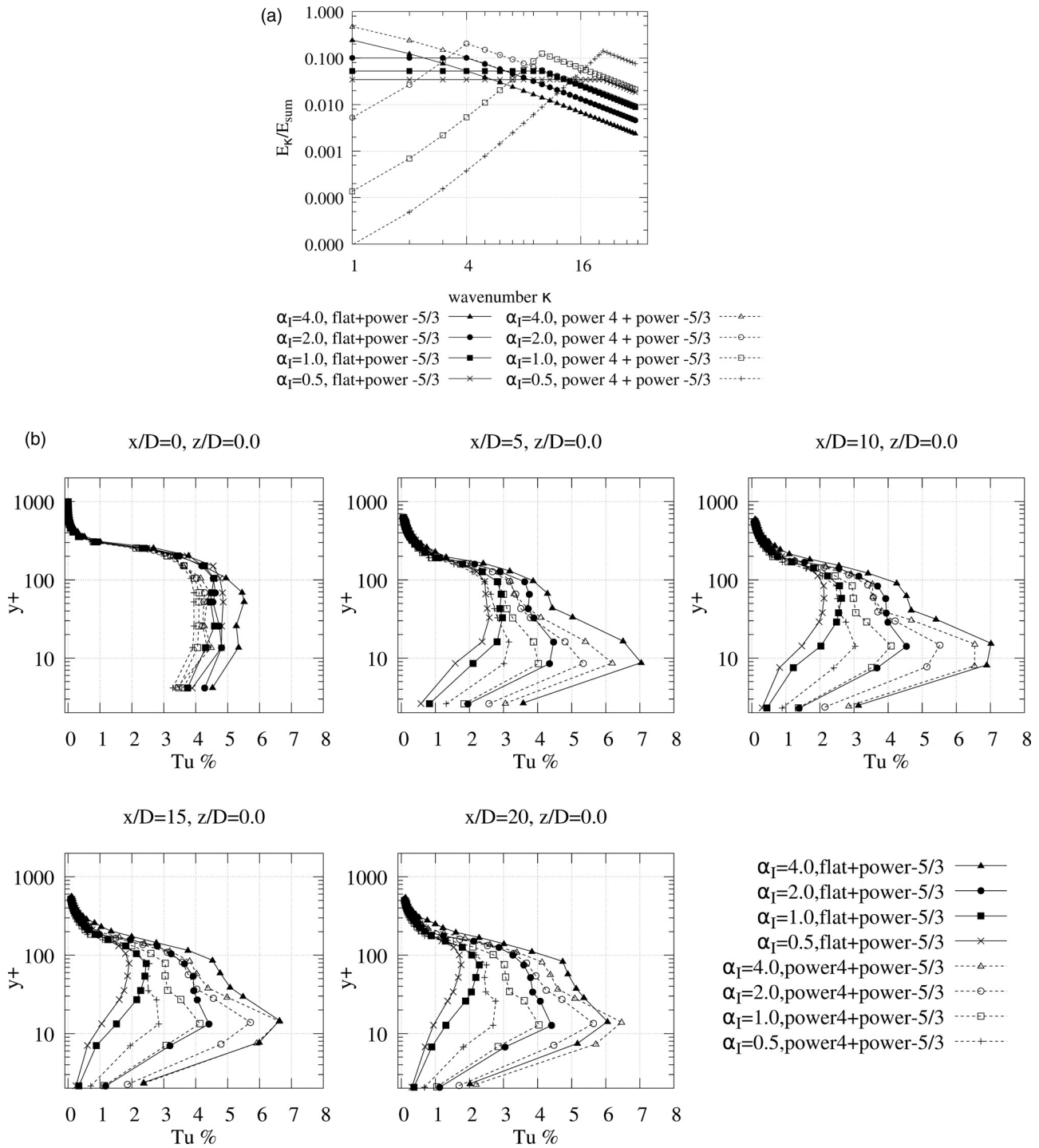


FIG. 17. The effect of the prescribed spectrum: (a) Spectrum controlled by α_I , (b) turbulence intensity of LES results.

inertial region, as shown in Fig. 17(a). Four α_I are discussed: 0.5, 1.0, 2.0, and 4.0. As shown in Fig. 17(b), $\alpha_I = 4.0$ on both approximated spectra can achieve the maximum turbulence intensity roughly as a constant. For those spectrum approximations with much shorter

inertial regions, the turbulence intensities decay more severely. This is caused by dissipation, as energy is mostly allocated to large wavenumbers. $\alpha_I = 0.5$ on a 4 power-law combined with a $-5/3$ power-law spectrum attains the minimum turbulence intensity. The criterion for

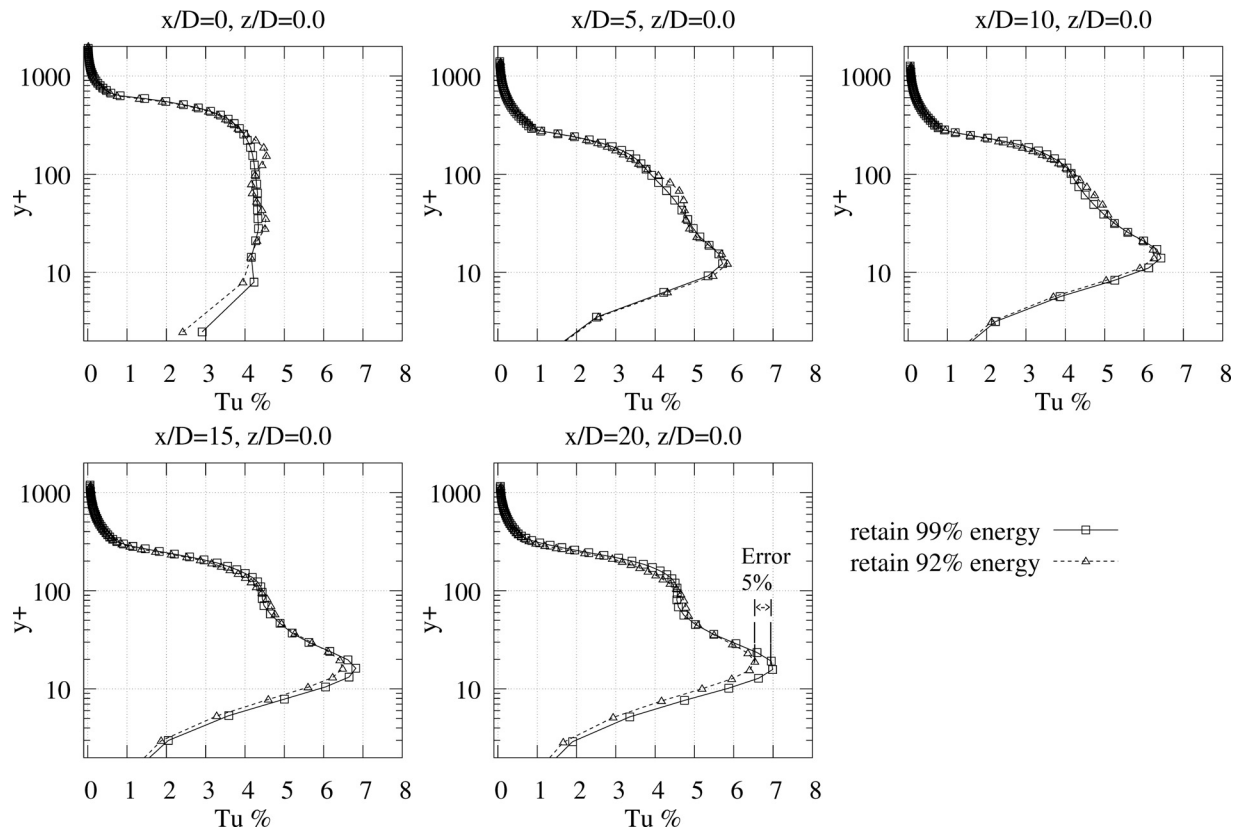


FIG. 18. Turbulence intensity of LES results.

choosing α_l is that a maximum turbulence kinetic energy can be attained as a constant. When using the optimum α_l , a 4 power-law combined with a $-5/3$ power-law spectrum approximation can be equivalent to a flat line combined with a $-5/3$ power-law spectrum approximation. In this case as an example, the optimal choice is the spectrum constructed by a flat line and a $-5/3$ power law when $\alpha_l = 4$.

4. Retained energy for retaining modes

A cutoff criterion based on the total energy is adopted when selecting eigenmodes. It is necessary to retain a sufficient fraction of the total energy of the signal while keeping the least retained eigenmodes. Figure 18 compares two choices of the energy retaining ratio. The method for choosing the retained energy ratio is to choose the smallest number of modes that should be big enough to retain the energy in the Reynolds stresses in the inflow. The criterion is no more 5% difference in turbulent kinetic energy far downstream of the inflow compared to the case where all modes are retained. As an example, Fig. 18 shows that retaining 92% energy results in an error of no more than 5% for most parts of turbulence intensity profiles. Meanwhile, no more than one-fifth of eigenmodes are preserved for a fraction of 92%. This helps to save the computational effort during LES simulation as at least four-fifths of eigenmodes are ignored. Therefore, 92% is selected as the energy retaining ratio.

C. Validation

The mean velocity profile in wall units is plotted in Fig. 19. The averages are taken in the z direction and in time t . The profile of LES results matches well with the logarithmic law $u^+ = 2.5 * \log(y^+) + 5$ from around $y^+ = 30$.

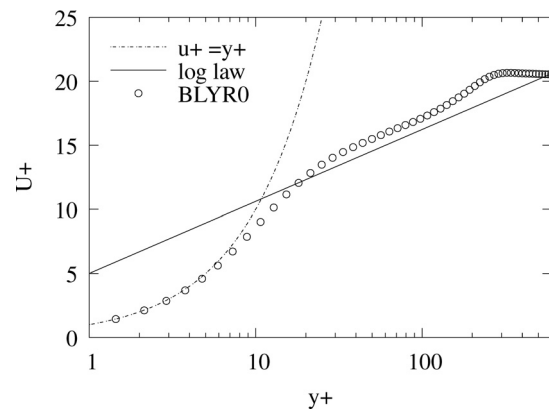
FIG. 19. Laterally averaged mean velocity profile of Spalart's $Re_\theta = 670$ case at $x/D = 16$.

Figure 20 shows the laterally averaged rms values of Reynolds normal stresses non-dimensionalized by u_τ , vs y/δ , which are compared with Spalart's DNS result at $Re_\theta = 670$. The LES curves agree well with Spalart's DNS curves reasonably. The LES turbulence intensities in the orthogonal directions v'^+ and w'^+ are slightly offset from the DNS data by a constant distance throughout the wall-normal direction. This might be caused by the dissipation induced by the numerical scheme inherent in the LES code. This good match

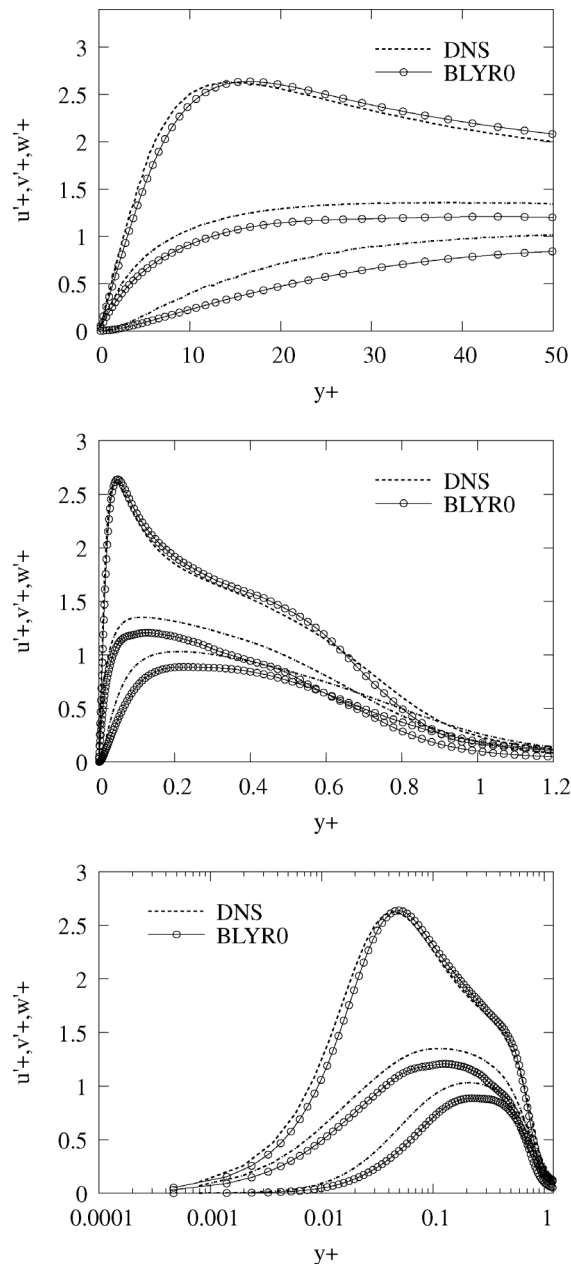


FIG. 20. Turbulence intensities of Spalart's $Re_\theta = 670$ case at $x/D = 16$.

confirms the validity of the synthetic inflow generator in the boundary layer case of a moderate Reynolds number.

To further visualize qualitative features of the inflow, Fig. 21 shows the fluctuation component of the streamwise velocity on the plane near the wall. The synthetic inflow generator is capable of regenerating streaks as in real flow just downstream from the inlet.

D. Computation time

All the filtered coefficients of modes are prepared before the main LES simulation. All the effort for synthesizing the inflow signal, at the stage of the main simulation, is the generation of a random sequence by the random number generator, which is only needed once every "inflow time step," as well as its following simple linear calculations.

Figure 22 shows the time needed for the inflow generator. This happens every t_{inflow} .

VI. CONCLUSIONS

This study presents a novel synthetic inflow generator capable of producing a random field matching a realistic set of two-point statistics with minimal input. The method constitutes two main elements, which are the preliminary data generator by RANS and the reconstruction of eigenmodes.

Compared with previous synthetic generation methods, the procedure proposed in this study is much more efficient for the following reasons. First, the preliminary simulation is tiny. A realistic approximation of correlations for use in the main simulation finishes within seconds. Second, all the efforts required for synthesizing the inflow signal, at the stage of the main simulation, are the random number generator, which does not need to update every time step, and convolution. All the filtered coefficients of modes are prepared before the main simulation. Third, the synthesizing is operated on a single two-dimensional slice, although 3D data are required. This is enabled by the filtering (the exponential function of the time filter) that correlates the current data with the data from the previous time step. Robustness and accuracy are improved because the proposed method guarantees the prescribed Reynolds stresses, the realistic length scales, and two-point and two-time correlations without resorting to a "decoupling tensor scaling."

Results prove that as long as controlling parameters needed are setup reasonably, the proposed synthetic generator can produce turbulence inflow, which is more close to realistic compared to other existing inflow generation methods. The inflow generator method can show a slight advantage over the periodic method in matching the DNS curve in the log-law region. The computed Reynolds normal

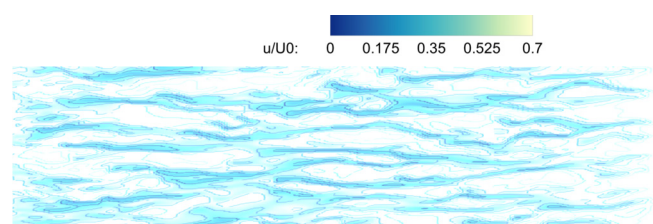


FIG. 21. The instantaneous velocity profiles at $y^+ = 15$ of the boundary layer flow.

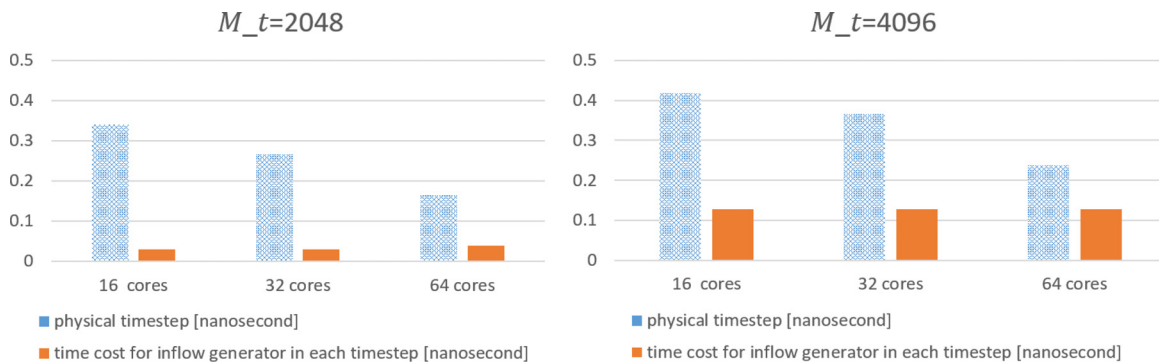


FIG. 22. Wall time for one time step when random sequence is updated for inflow generation.

stresses can match well with the DNS result, with the error minimized when the energy spectrum, the time filter support, and the t_{inflow} are specified as optimum. Compared with other methods (including Batten's and SEM), the regeneration of the Reynolds shear stress by the proposed inflow generator can collapse onto the reference data more quickly with better matching. This is mainly because, rather than using uniform length scales for different heights as in other methods, the proposed synthetic inflow generator specifies realistic length scales for corresponding heights, which are estimated from the preliminary EARSIM calculation.

The general guidance for new users is provided on how to select related parameters for using the proposed synthetic inflow generator. The criteria for setting up the parameters needed are provided. The number of Fourier modes specified in the spanwise direction N_f should be selected as three to four times the number of large structures in the spanwise direction of the domain. The minimum number of samples for interpolation in the spanwise direction N_z should be $N_z \geq 2N_f$. The time filter support M_t should be chosen as a value that results in a decay time longer than the estimated integral length scale. A controlling factor α_t used to control the specified spectrum shape should satisfy the criterion that a maximum turbulence kinetic energy can be attained as a constant. When using the optimum α_t , a 4 power law combined with a $-5/3$ power law spectrum approximation can be equivalent to a flat line combined with a $-5/3$ power law spectrum approximation. The retained energy ratio when selecting eigenmodes should be selected to retain a sufficient fraction of the total energy of the signal while keeping the least retained eigenmodes. The criterion is no more 5% difference in turbulent kinetic energy far downstream of the inflow compared to the case where all modes are retained.

The synthesized instantaneous inlet flow field is applicable to inhomogeneous (at least in the streamwise and the wall-normal directions) wall-bounded flows.

The proposed inflow generator shows potential for more complex applications, as the mode preparation and mode interpolation during the preliminary procedure does not limit the shape or the meshing type of the inlet slice. The proposed synthetic inflow generation will be able to make contributions to complex geometries or industrial applications where it may be difficult to setup auxiliary simulations with periodic boundaries or find any source of library data. The authors would recommend applying the proposed inflow generator to a wide range of turbomachinery cases such as film cooling flows.

ACKNOWLEDGMENTS

This work was funded by Rolls-Royce plc. Rolls-Royce plc is gratefully acknowledged for supporting this work and for granting permission for its publication. The authors sincerely thank Aerothermal Specialist Haidong Li in Rolls-Royce plc for helpful suggestions on the paper review. The authors also acknowledge the use of the University of Oxford Advanced Research Computing (ARC) facility in carrying out this work (<http://dx.doi.org/10.5281/zenodo.22558>). Part of this work was also performed using resources provided by the Cambridge Service for Data Driven Discovery (CSD4) operated by the University of Cambridge Research Computing Service (www.csd3.cam.ac.uk), provided by Dell EMC and Intel using Tier-2 funding from the Engineering and Physical Sciences Research Council (Capital Grant No. EP/T022159/1), and DiRAC funding from the Science and Technology Facilities Council (www.dirac.ac.uk).

AUTHOR DECLARATIONS

Conflict of Interest

The authors have no conflicts to disclose.

Author Contributions

Muting Hao: Conceptualization (equal); Data curation (equal); Formal analysis (equal); Investigation (equal); Methodology (equal); Software (equal); Validation (equal); Visualization (equal); Writing – original draft (equal); Writing – review & editing (equal). **Joshua Hope-collins:** Investigation (supporting); Software (equal). **Luca di Mare:** Conceptualization (equal); Funding acquisition (equal); Investigation (equal); Methodology (equal); Project administration (equal); Software (equal); Supervision (equal); Writing – review & editing (equal).

DATA AVAILABILITY

The data that support the findings of this study are available from the corresponding author upon reasonable request.

NOMENCLATURE

C	Constant
$c(\tau)$	Correlation coefficient

dt_{inflow}	The “inflow time step”	$\bar{u}(y, z)$	Mean streamwise velocity
f_{κ}	The ratio of discrete signal energy to the energy summation on the approximate spectrum	U^+	Velocity in wall units
f_{κ}^0	Correlation coefficient, $f_{\kappa}^0 = 1$	U_k	Mean velocity in tensor notation, k 1: streamwise direction, $k = 2$, wall-normal direction, $k = 3$, spanwise direction
F	The summation of energy on the approximate spectrum	$\langle u'u' \rangle_{\kappa}(y_1, y_2)$	The covariance component constructed by the u' of y_1 and the u' of y_2
F_1, F_2, F_3, F_4	Scaling factor	$\langle u'v' \rangle_{\kappa}(y_1, y_2)$	The covariance component constructed by the u' of y_1 and the v' of y_2
g_i^j	The i th row of the j th eigenvector	v	Velocity in the wall-normal direction
i, j, k	Integer	v'	Turbulent velocity in the wall-normal direction
k_e	The kinetic energy of turbulent fluctuations per unit mass	$\hat{v}_j(y)$	The constructed velocity on an individual point of the median plane in the wall-normal direction
k_i	The kinetic energy retained in the i th eigenmode	v'^+	Turbulent intensity in the wall-normal direction in wall units
k_l	Constant	$\tilde{v}_j(y, z)$	The wall-normal velocity component of the j th scaled eigenvector at the position (y, z)
l_x	The streamwise wavenumber	$v'(y, z)$	A random correlated $(y-z)$ velocity in the wall-normal direction
$\ell(y_i)$	The length scale at the normal-wall position y_i	$\tilde{v}_{jk}(y, z)$	The wall-normal velocity component of the uncorrelated constructed signal
m	The number of the retained eigenmodes	$\bar{v}(y, z)$	Mean wall-normal velocity
M	The assembled covariance tensor	$\langle v'v' \rangle_{\kappa}(y_1, y_2)$	The covariance component constructed by the v' of y_1 and the v' of y_2
M_t	Time filter support	w	Velocity in the spanwise direction
n	The number of nodes in the wall-normal direction	w'	Turbulent velocity in the spanwise direction
N	The number of spanwise Fourier harmonics	$\hat{w}_j(y)$	The constructed velocity on an individual point of the median plane in the spanwise direction
N_f	The number of Fourier modes specified in the spanwise direction	$\tilde{w}_j(y, z)$	The spanwise velocity component of the j th scaled eigenvector at the position (y, z)
N_I	The dividing wavenumber	$w'(y, z)$	A random correlated $(y-z)$ velocity in the spanwise direction
N_z	The number of samples for interpolation in the spanwise direction	$\bar{w}(y, z)$	Mean wall-spanwise velocity
Nu_0	Freestream kinematic viscosity	$\tilde{w}_{jk}(y, z)$	The spanwise velocity component of the uncorrelated constructed signal
p_{ij}	The transformation matrix	w'^+	Turbulent intensity in the spanwise direction in wall units
q_{ij}	The covariance matrix	$\langle w'w' \rangle_{\kappa}(y_1, y_2)$	The covariance component constructed by the w' of y_1 and the w' of y_2
$r_{jkl}(t)$	A random complex variable	W	The width of the inlet slice
R_{uu}	Covariance components related to $u'u'$	x	Coordinate/distance in the streamwise direction
R_{uv}	Covariance components related to $u'v'$	x_i^*	An uncorrelated random variable
R_{vv}	Covariance components related to $v'v'$	x^+	Streamwise distance in wall units
R_{ww}	Covariance components related to $w'w'$	X_k	Position vector in tensor notation, $k = 1$: streamwise direction, $k = 2$, wall-normal direction, $k = 3$, spanwise direction
Re	Reynolds number	y	Coordinate/distance in the wall-normal direction
Re_{θ}	Reynolds number by momentum thickness	y_i^*	An correlated random variable
Re_{τ}	Viscous Reynolds number	y^+	The distance to the wall in wall units
$\mathbb{R}^{n \times n}$	A matrix of n by n	y_0	First grid normal space to the wall
s_{ij}^*	The factorization matrix	y_1, y_2	Wall-normal positions
$s_{jk}(t)$	A correlated random factor	z	Coordinate/distance in the spanwise direction
S_{ij}	Mean strain-rate tensor	z^+	Spanwise distance in wall units
t	Time	α	Coefficient
Tu	Turbulence intensity	α_t	The time filter control parameter
u	Freestream velocity in the streamwise direction	α_I	The spectrum control parameter
u'^+	Turbulent intensity in the streamwise direction in wall units	β^*	Constant
u'	Turbulent velocity in the streamwise direction		
u_0	Velocity in the streamwise direction		
$\hat{u}_j(y)$	The constructed velocity on an individual point of the median plane in the streamwise direction		
$\tilde{u}_j(y, z)$	The streamwise velocity component of the j th scaled eigenvector at the position (y, z)		
\bar{u}_i	Mean velocity		
u_{τ}	Friction velocity		
$u'(y, z)$	A random correlated $(y-z)$ velocity in the streamwise direction		
$\tilde{u}_{jk}(y, z)$	The streamwise velocity component of the uncorrelated constructed signal		

γ	Specific-heat ratio, c_p/c_v
Δx^+	The grid size in the streamwise direction in wall units
Δy^+	The grid size in the normal-wall direction in wall units
Δz^+	The grid size in the spanwise direction in wall units
Δt	The time separation that corresponds to two consecutive samples
δ	Channel half height
δ_{ij}	Kronecker delta
δ^*	Boundary layer displacement thickness
δ_{99}	Turbulent boundary layer thickness
μ_T	Eddy viscosity
λ_i	The eigenvalue of the i th eigenmode
θ	Momentum thickness
κ	The spanwise Fourier mode index
ρ	Density
τ_{jk}	A timescale associated with mode jk
τ_{ij}^0	Specific Reynolds stress tensor
ψ_{jkl}	The digital filter
Ω_{kj}	Mean-rotation tensor
ω	Specific dissipation rate
-1	The time index

REFERENCES

- ¹A. Altıntaş, L. Davidson, and S.-H. Peng, "Direct numerical simulation of drag reduction by spanwise oscillating dielectric barrier discharge plasma force," *Phys. Fluids* **32**, 075101 (2020).
- ²M. E. Nakhchi, S. W. Naung, and M. Rahmati, "DNS of secondary flows over oscillating low-pressure turbine using spectral/hp element method," *Int. J. Heat Fluid Flow* **86**, 108684 (2020).
- ³L. Ottolenghi, C. Adduce, F. Roman, and G. la Forgia, "Large eddy simulations of solitons colliding with intrusions," *Phys. Fluids* **32**, 096606 (2020).
- ⁴H. Abdulrahman, A. Validi, and F. Jaber, "Large-eddy simulation/filtered mass density function of non-premixed and premixed colorless distributed combustion," *Phys. Fluids* **33**, 055118 (2021).
- ⁵S. Katiyar and S. Sarkar, "Flow transition on the suction surface of a controlled-diffusion compressor blade using a large-eddy simulation," *Phys. Fluids* **34**, 094108 (2022).
- ⁶P. Batten, U. Goldberg, and S. Chakravarthy, "Interfacing statistical turbulence closures with large-eddy simulation," *AIAA J.* **42**, 485–492 (2004).
- ⁷N. Jarrin, S. Benhamadouche, D. Laurence, and R. Prosser, "A synthetic-eddy-method for generating inflow conditions for large-eddy simulations," *Int. J. Heat Fluid Flow* **27**, 585–593 (2006).
- ⁸N. Jarrin, R. Prosser, J.-C. Uribe, S. Benhamadouche, and D. Laurence, "Reconstruction of turbulent fluctuations for hybrid RANS/LES simulations using a synthetic-eddy method," *Int. J. Heat Fluid Flow* **30**, 435–442 (2009).
- ⁹N. S. Dhamankar, G. A. Blaisdell, and A. S. Lyrintzis, "Overview of turbulent inflow boundary conditions for large-eddy simulations," *AIAA J.* **56**, 1317–1334 (2018).
- ¹⁰H. F. Fasel, U. Rist, and U. Konzelmann, "Numerical investigation of the three-dimensional development in boundary-layer transition," *AIAA J.* **28**, 29–37 (1990).
- ¹¹T. Sayadi, C. W. Hamman, and P. Moin, "Direct numerical simulation of complete H-type and K-type transitions with implications for the dynamics of turbulent boundary layers," *J. Fluid Mech.* **724**, 480–509 (2013).
- ¹²X. Gloerfelt and J. Berland, "Direct computation of turbulent boundary layer noise," AIAA Paper No. AIAA 2009-3401, 2009.
- ¹³M. L. Shur, P. R. Spalart, M. K. Strelets, and A. K. Travin, "Synthetic turbulence generators for RANS-LES interfaces in zonal simulations of aerodynamic and aeroacoustic problems," *Flow, Turbul. Combust.* **93**, 63–92 (2014).
- ¹⁴T. Blackmore, W. M. Batten, and A. S. Bahaj, "Inlet grid-generated turbulence for large-eddy simulations," *Int. J. Comput. Fluid Dyn.* **27**, 307–315 (2013).
- ¹⁵X. I. A. Yang, J. Sadique, R. Mittal, and C. Meneveau, "Integral wall model for large eddy simulations of wall-bounded turbulent flows," *Phys. Fluids* **27**, 025112 (2015).
- ¹⁶P. Schlatter, R. Örlü, Q. Li, G. Brethouwer, J. H. M. Fransson, A. V. Johansson, P. H. Alfredsson, and D. S. Henningson, "Turbulent boundary layers up to $Re_\theta = 2500$ studied through simulation and experiment," *Phys. Fluids* **21**, 051702 (2009).
- ¹⁷N. J. Mullenix, D. V. Gaitonde, and M. R. Visbal, "Spatially developing supersonic turbulent boundary layer with a body-force-based method," *AIAA J.* **51**, 1805–1819 (2013).
- ¹⁸P. R. Spalart and A. Leonard, "Direct numerical simulation of equilibrium turbulent boundary layers," in *Turbulent Shear Flows 5* (Springer, Berlin, Heidelberg, 1987), pp. 234–252.
- ¹⁹T. S. Lund, X. Wu, and K. D. Squires, "Generation of turbulent inflow data for spatially-developing boundary layer simulations," *J. Comput. Phys.* **140**, 233–258 (1998).
- ²⁰G. Tabor and M. Baba-Ahmadi, "Inlet conditions for large eddy simulation: A review," *Comput. Fluids* **39**, 553–567 (2010).
- ²¹B. Morgan, J. Larsson, S. Kawai, and S. K. Lele, "Improving low-frequency characteristics of recycling/rescaling inflow turbulence generation," *AIAA J.* **49**, 582–597 (2011).
- ²²L. Duan, M. M. Choudhari, and M. Wu, "Numerical study of acoustic radiation due to a supersonic turbulent boundary layer," *J. Fluid Mech.* **746**, 165–192 (2014).
- ²³M. M. Rai and P. Moin, "Direct numerical simulation of transition and turbulence in a spatially evolving boundary layer," *J. Comput. Phys.* **109**, 169–192 (1993).
- ²⁴S. Hanna, S. Tehrani, B. Carissimo, R. Macdonald, and R. Lohner, "Comparisons of model simulations with observations of mean flow and turbulence within simple obstacle arrays," *Atmos. Environ.* **36**, 5067–5079 (2002).
- ²⁵K. Kondo, S. Murakami, and A. Mochida, "Generation of velocity fluctuations for inflow boundary condition of LES," *J. Wind Eng. Ind. Aerodyn.* **6768**, 51–64 (1997).
- ²⁶S. Lee, S. K. Lele, and P. Moin, "Simulation of spatially evolving turbulence and the applicability of Taylor's hypothesis in compressible flow," *Phys. Fluids A* **4**, 1521–1530 (1992).
- ²⁷H. Le, P. Moin, and J. Kim, "Direct numerical simulation of turbulent flow over a backward-facing step," *J. Fluid Mech.* **330**, 349–374 (1997).
- ²⁸A. Keating, U. Piomelli, E. Balaras, and H.-J. Kaltenbach, "A priori and a posteriori tests of inflow conditions for large-eddy simulation," *Phys. Fluids* **16**, 4696–4712 (2004).
- ²⁹B. Roidl, M. Meinke, and W. Schröder, "A reformulated synthetic turbulence generation method for a zonal RANS-LES method and its application to zero-pressure gradient boundary layers," *Int. J. Heat Fluid Flow* **44**, 28–40 (2013).
- ³⁰A. Smirnov, S. Shi, and I. Celik, "Random flow generation technique for large eddy simulations and particle-dynamics modeling," *J. Fluids Eng.* **123**, 359–371 (2001).
- ³¹P. Druault, E. Lamballais, J. Delville, and J.-P. Bonnet, "Development of experiment/simulation interfaces for hybrid turbulent results analysis via the use of DNS," in *First Symposium on Turbulence and Shear Flow Phenomena* (Begell House Inc., 1999).
- ³²G. Berkooz, P. Holmes, and J. L. Lumley, "The proper orthogonal decomposition in the analysis of turbulent flows," *Annu. Rev. Fluid Mech.* **25**, 539–575 (1993).
- ³³M. Klein, A. Sadiki, and J. Janicka, "A digital filter based generation of inflow data for spatially developing direct numerical or large eddy simulations," *J. Comput. Phys.* **186**, 652–665 (2003).
- ³⁴Z.-T. Xie and I. P. Castro, "Efficient generation of inflow conditions for large eddy simulation of street-scale flows," *Flow, Turbul. Combust.* **81**, 449–470 (2008).
- ³⁵J. Hœpfner, Y. Naka, and K. Fukagata, "Realizing turbulent statistics," *J. Fluid Mech.* **676**, 54–80 (2011).
- ³⁶J. P. Bonnet, D. R. Cole, J. Delville, M. N. Glauser, and L. S. Ukeiley, "Stochastic estimation and proper orthogonal decomposition: Complementary techniques for identifying structure," *Exp. Fluids* **17**, 307–314 (1994).

- ³⁷D. C. Wilcox and M. W. Rubesin, "Progress in turbulence modeling for complex flow fields including effects of compressibility," Report No. NASA-TP-1517 (NASA, 1980).
- ³⁸A. Nawab and L. di Mare, " Re_τ scaling of POD modes in plane channel flow," *Phys. Fluids* **30**, 055109 (2018).
- ³⁹P. S. Klebanoff, "Characteristics of turbulence in a boundary layer with zero pressure gradient," Technical Report No. NACA-TN-3178 (National Advisory Committee for Aeronautics, 1954).
- ⁴⁰M. Fathali, M. Klein, T. Broeckhoven, C. Lacor, and M. Baelmans, "Generation of turbulent inflow and initial conditions based on multi-correlated random fields," *Int. J. Numer. Methods Fluids* **57**, 93–117 (2008).
- ⁴¹L. di Mare, M. Klein, W. P. Jones, and J. Janicka, "Synthetic turbulence inflow conditions for large-eddy simulation," *Phys. Fluids* **18**, 025107 (2006).
- ⁴²A. Kempf, M. Klein, and J. Janicka, "Efficient generation of initial- and inflow-conditions for transient turbulent flows in arbitrary geometries," *Flow, Turbul. Combust.* **74**, 67–84 (2005).
- ⁴³J. A. B. Wills, "On convection velocities in turbulent shear flows," *J. Fluid Mech.* **20**, 417–432 (1964).
- ⁴⁴M. Hao, F. Wang, J. Hope-Collins, M. E. Rife, and L. di Mare, "Template-based hexahedral mesh generation for turbine cooling geometries," in *Volume 2C: Turbomachinery* (American Society of Mechanical Engineers, 2020).
- ⁴⁵M. Lee and R. D. Moser, "Direct numerical simulation of turbulent channel flow up to $Re_\tau = 590$," *J. Fluid Mech.* **774**, 395–415 (2015).
- ⁴⁶S. Pirozzoli and P. Orlandi, "Natural grid stretching for DNS of wall-bounded flows," *J. Comput. Phys.* **439**, 110408 (2021).
- ⁴⁷H. Choi and P. Moin, "Effects of the computational time step on numerical solutions of turbulent flow," *J. Comput. Phys.* **113**, 1–4 (1994).